Matter ejections behind the highs and lows of the transitional millisecond pulsar PSR J1023+0038

M. C. Baglio[1,2], F. Coti Zelati[3,4,2,★], S. Campana[2], G. Busquet[5,6,4], P. D'Avanzo[2], S. Giarratana[7,8], M. Giroletti[7,8], F. Ambrosino[9,10,11], S. Crespi[1], A. Miraval Zanon[12,9], X. Hou[13,14], D. Li[15,16,17], J. Li[18,19], P. Wang[20], D. M. Russell[1], D. F. Torres[3,4,21], K. Alabarta[1], P. Casella[9], S. Covino[2], D. M. Bramich[1,22], D. de Martino[23], M. Méndez[24], S. E. Motta[2], A. Papitto[9], P. Saikia[1], and F. Vincentelli[25,26]

[1] Center for Astro, Particle, and Planetary Physics, New York University Abu Dhabi, P.O. Box 129188, Abu Dhabi, UAE
e-mail: mcb19@nyu.edu
[2] INAF–Osservatorio Astronomico di Brera, Via Bianchi 46, I-23807 Merate (LC), Italy
[3] Institute of Space Sciences (ICE, CSIC), Campus UAB, Carrer de Can Magrans s/n, E-08193 Barcelona, Spain
e-mail: cotizelati@ice.csic.es
[4] Institut d'Estudis Espacials de Catalunya (IEEC), Carrer Gran Capità 2–4, E-08034 Barcelona, Spain
[5] Departament de Física Quàntica i Astrofísica, Universitat de Barcelona (UB), c/ Martí Franquès 1, E-08028 Barcelona, Spain
[6] Institut de Ciències del Cosmos (ICCUB), Universitat de Barcelona (UB), c/ Martí Franquès 1, E-08028 Barcelona, Spain
[7] INAF–Istituto di Radioastronomia, via Gobetti 101, I-40129, Bologna, Italy
[8] Department of Physics and Astronomy, University of Bologna, via Gobetti 93/2, I-40129 Bologna, Italy
[9] INAF–Osservatorio Astronomico di Roma, Via Frascati 33, I-00078 Monteporzio Catone (RM), Italy
[10] INAF–Istituto di Astrofisica e Planetologia Spaziali, Via Fosso del Cavaliere 100, I-00133 Rome, Italy
[11] Sapienza Università di Roma, Piazzale Aldo Moro 5, I-00185 Rome, Italy
[12] ASI - Agenzia Spaziale Italiana, Via del Politecnico snc, I-00133 Rome, Italy
[13] Yunnan Observatories, Chinese Academy of Sciences, 650216 Kunming, China
[14] Key Laboratory for the Structure and Evolution of Celestial Objects, Chinese Academy of Sciences, Kunming 650216, China
[15] National Astronomical Observatories, Chinese Academy of Sciences, 20A Datun Road, Chaoyang District, Beijing, 100101, China
[16] University of Chinese Academy of Sciences, Beijing, 100049, China
[17] Research Center for Intelligent Computing Platforms, Zhejiang Laboratory, Hangzhou, 311100, China
[18] CAS Key Laboratory for Research in Galaxies and Cosmology, Department of Astronomy, University of Science and Technology of China, Hefei, China
[19] School of Astronomy and Space Science, University of Science and Technology of China, Hefei, China
[20] Institute for Frontiers in Astronomy and Astrophysics, Beijing Normal University, Beijing, 102206, China
[21] Institució Catalana de Recerca i Estudis Avançats (ICREA), Passeig Lluís Companys 23, E-08010 Barcelona, Spain
[22] Division of Engineering, New York University Abu Dhabi, P.O. Box 129188, Saadiyat Island, Abu Dhabi, UAE
[23] INAF−-Osservatorio Astronomico di Capodimonte, Salita Moiariello 16, I-80131 Napoli, Italy
[24] Kapteyn Astronomical Institute, University of Groningen, PO BOX 800, NL-9700 AV Groningen, The Netherlands
[25] Instituto de Astrofísica de Canarias, E-38205 La Laguna, Tenerife, Spain
[26] Departamento de Astrofísica, Universidad de La Laguna, E-38206 La Laguna, Tenerife, Spain

ABSTRACT

Transitional millisecond pulsars are an emerging class of sources linking low-mass X-ray binaries to millisecond radio pulsars in binary systems. These pulsars alternate between a radio pulsar state and an active low-luminosity X-ray disc state. During the active state, these sources exhibit two distinct emission modes (high and low) that alternate unpredictably, abruptly, and incessantly. X-ray to optical pulsations are observed only during the high mode. Knowledge of the root reason for this puzzling behaviour remains elusive. This paper presents the results of the most extensive multi-wavelength campaign ever conducted on the transitional pulsar prototype, PSR J1023+0038, covering from radio to X-rays. The campaign was carried out over two nights in June 2021, and involved 12 different telescopes and instruments including *XMM-Newton*, *HST*, *VLT*/FORS2 (in polarimetric mode), *ALMA*, *VLA* and *FAST*. By modelling the broadband spectral energy distributions in both emission modes, we show that the mode switches are caused by changes in the innermost region of the accretion disc. These changes trigger the emission of discrete mass ejections, which occur on top of a compact jet, as testified by the detection of at least one short-duration millimetre flare with ALMA at the high-to-low mode switch. A subsequent re-enshrouding of the pulsar completes the scenario behind the mode switches.

Key words. accretion, accretion disks – ISM: jets and outflows – pulsars: general – radio continuum: stars – stars: neutron – X-rays: binaries

1. Introduction

The evolutionary path that leads a neutron star (NS) in a low-mass X-ray binary system to become a millisecond radio pulsar

---

★ The first two authors equally contributed to this work.

passes through different stages, the most enigmatic of which is represented by transitional millisecond pulsars (tMSPs). These sources alternate between a radio pulsar state and an active low-luminosity X-ray disc state on timescales from weeks to months (for reviews, see Campana & Di Salvo 2018; Papitto & de Martino 2022). The archetypal tMSP is PSR J1023+0038 (hereafter referred to as J1023), which was discovered in 2007 as a 1.69 ms radio pulsar orbiting a low-mass ($\simeq 0.2\,M_\odot$) companion star with a period of 4.75 hr (Archibald et al. 2009). In 2013, J1023 showed a sudden brightening in the emission at X-ray and gamma-ray frequencies (by a factor of 5–10) as well as at ultraviolet (UV) and optical frequencies (by 1–2 mag), along with the disappearance of the pulsed radio signal (Stappers et al. 2014; Patruno et al. 2014). Double-peaked optical emission lines were soon detected, indicating the formation of an accretion disc (Coti Zelati et al. 2014). J1023 has remained in this active state ever since, at an X-ray luminosity of $L_X \simeq 7 \times 10^{33}$ erg s^{-1} in the 0.3–80 keV energy range (Coti Zelati et al. 2018) for a distance of 1.37 kpc (Deller et al. 2012).

During the sub-luminous X-ray state, the X-ray emission of J1023 is observed to switch between two distinct intensity modes, dubbed high and low, with sporadic flares in between. The high mode occurs 70–80% of the time, while the low mode occurs 20–30% of the time and typically lasts from a few tens of seconds to minutes. The drop and rise timescales involved in the mode switching are of the order of ≈ 10 s. X-ray, UV and optical pulsations occur simultaneously in the X-ray high-intensity mode, and disappear in the low mode (Archibald et al. 2015; Papitto et al. 2019; Miraval Zanon et al. 2022; Illiano et al. 2023). The UV, optical, and near infrared emission is dominated by the accretion disc and irradiated companion star and also shows flaring and flickering activities (Shahbaz et al. 2015; Kennedy et al. 2018; Papitto et al. 2018; Hakala & Kajava 2018; Shahbaz et al. 2018). Optical polarimetric observations reveal a linear polarisation at a level of ~1% (Baglio et al. 2016; Hakala & Kajava 2018) of uncertain origin. Bright, variable radio continuum emission is also detected (Deller et al. 2015). In particular, the low X-ray mode episodes are accompanied by an increase of the radio flux by a factor of $\simeq 3$ on average, with fairly equal rise and decay times and an overall duration that matches low X-ray mode intervals (Bogdanov et al. 2018, see also Fig. 1). These rebrightenings are associated with a temporal evolution of the radio spectrum from inverted to steep. Currently, J1023 spins down at a rate that is $\simeq 4\%$ faster than in the radio pulsar state (Burtovoi et al. 2020). This overall behaviour is unique in the landscape of X-ray binaries and still defies a comprehensive explanation.

This paper presents the results of the largest multiwavelength campaign ever performed on J1023. Our aim is to ultimately understand the root cause of the mode changes in the active sub-luminous X-ray state and the implication for our understanding of the accretion-ejection coupling in X-ray binary systems harboring rapidly spinning NSs. The observations of our campaign were conducted on two different nights in June 2021. The first night (Night 1) involved *XMM-Newton*, the Nuclear Spectroscopic Telescope Array (*NuSTAR*), the Hubble Space Telescope (*HST*), the Son OF ISAAC (SOFI) instrument mounted on the New Technology Telescope (NTT), the Karl G. Jansky Very Large Array (VLA) and the Fivehundred-meter Aperture Spherical Telescope (FAST); the second night (Night 2) involved the Neutron Star Interior Composition Explorer Mission (*NICER*), the Neil Gehrels Swift Observatory (*Swift*), the Very Large Telescope (VLT), the Rapid Eye Mount (REM) telescope and the Atacama Large millimetre/submillimetre Array (ALMA). The paper is structured as fol-

lows: in Sect. 2, we present the observations and data analysis. The results are then reported in Sect. 3. In Sect. 4, we propose a scenario for the mode switching, present the results of the modelling of the spectral energy distributions (SEDs) in the two modes, and discuss the results in relation to our scenario. Conclusions follow in Sect. 5.

2. Observations and data analysis

Table 1 lists all the observations of J1023 presented in this paper. In the following, we describe these observations and the procedures adopted to process and analyse these data.

2.1. XMM-Newton (Night 1)

XMM-Newton (Jansen et al. 2001; Schartel et al. 2022) observed J1023 on 2021 June 3–4 (Obs ID. 0864010101) using the European Photon Imaging Cameras (EPIC) and the Optical/UV Monitor telescope (OM; Mason et al. (2001)). The EPIC-pn (Strüder et al. 2001) was set in fast timing mode (time resolution of 29.52 µs), the two EPIC-MOS (Turner et al. 2001) in full frame mode (time resolution of 2.6 s) and the OM in the fast window mode (time resolution of 0.5 s) with the *B* filter (effective wavelength 4330 Å; full-width at half-maximum 926 Å). The Observation Data Files were processed and analysed using the Science Analysis System (SAS; v. 20.0). The X-ray data were analysed in the same way as described by Miraval Zanon et al. (2022). No periods of high background activity were detected. The background-subtracted light curve was extracted over the time interval during which all three EPIC instruments collected data simultaneously and was binned with a time resolution of 10 s. The optical background-subtracted light curve was extracted using the OMFCHAIN pipeline with default parameters. The light curve was binned at a time resolution of 120 s to ensure a high SNR and detect any changes in the optical brightness at least during prolonged periods of low X-ray mode. The net count rates were then converted to magnitudes in the Vega system using the formula provided on the *XMM-Newton* online threads[1]. To align the X-ray and optical light curves with those extracted from other observatories, the arrival times of photons were converted from the Terrestrial Time (TT) standard to the Coordinated Universal Time (UTC) standard without applying a barycentric correction[2].

2.2. NuSTAR (Night 1)

NuSTAR (Harrison et al. 2013) observed J1023 for a total of ~48.6 ks and a net exposure of ~22 ks (Obs ID. 30601005002), almost fully overlapping with the *XMM-Newton* observation. Data were processed and analysed using the NuSTAR Data Analysis Software (NUSTARDAS, v.2.1.2) with the instrumental calibration files stored in CALDB v20220525 and the same prescriptions reported by Miraval Zanon et al. (2022). J1023 was detected up to energies of ~50 keV in both focal plane modules (FPMA and FPMB). Light curves were extracted separately for the two modules, combined to increase the SNR, and binned at a time resolution of 50 s.

---

[1] https://www.cosmos.esa.int/web/xmm-newton/sas-watchout-uvflux

[2] This same procedure was also applied to the data collected with *NuSTAR*, *Swift* and *NICER* presented in the following.

Table 1. Observation Log of J1023 in June 2021. Observations are listed in order of decreasing observing frequency.

Telescope/Instrument	Obs. ID/Project	Start – End time MMM DD hh:mm:ss (UTC)	Exposure (ks)	Band (setup)
		Night 1		
XMM-Newton/EPIC-pn	0864010101	Jun 3 20:44:32 – Jun 4 13:39:15	58.7	0.3–10 keV (fast timing)
XMM-Newton/EPIC-MOS1	0864010101	Jun 3 21:09:37 – Jun 4 13:39:01	58.1	0.3–10 keV (full frame)
XMM-Newton/EPIC-MOS2	0864010101	Jun 3 22:31:54 – Jun 4 13:39:02	53.5	0.3–10 keV (full frame)
NuSTAR/FPMA/FPMB	30601005002	Jun 3 20:36:09 – Jun 4 10:06:09	22.3/22.1	3–79 keV
Swift/XRT	00033012207	Jun 3 18:29:46 – Jun 3 23:45:44	6.4	0.3–10 keV (photon counting)
Swift/XRT	00033012208	Jun 4 02:27:57 – Jun 4 12:17:45	9.5	0.3–10 keV (photon counting)
Swift/XRT	00033012209	Jun 4 03:50:46 – Jun 4 08:44:56	2.0	0.3–10 keV (photon counting)
Swift/UVOT	00033012207	Jun 3 18:29:50 – Jun 3 23:45:46	6.3	UVM2 (Event)
Swift/UVOT	00033012209	Jun 4 03:50:50 – Jun 4 08:44:58	1.9	UVM2 (Event)
HST STIS/NUV-MAMA	16061	Jun 4 00:09:07 – Jun 4 00:43:27	2.1	G230L (fast timing spectroscopy)
HST STIS/NUV-MAMA	16061	Jun 4 01:35:28 – Jun 4 02:20:18	2.7	G230L (fast timing spectroscopy)
XMM-Newton/OM	0864010101	Jun 3 22:51:01 – Jun 4 13:23:52	48.4	*B* (fast window)
NTT/SOFI		Jun 3 23:49:09 – Jun 4 02:42:38	10.4	*J* (fast photometry)
VLA	SJ6401	Jun 3 22:30:00 – Jun 4 02:29:20	6.7	Band *X* (C configuration)
FAST	PT2020_0044	Jun 4 08:47:45 – Jun 4 11:47:45	10.8	Band *L*
		Night 2		
NICER/XTI	4034060102	Jun 26 21:56:04 – Jun 26 22:34:31	2.0	0.3–10 keV
NICER/XTI	4034060103	Jun 26 23:29:04 – Jun 27 01:33:51	4.1	0.3–10 keV
Swift/XRT	00033012214	Jun 26 22:19:35 – Jun 26 22:39:47	1.2	0.3–10 keV (photon counting)
Swift/XRT	00033012213	Jun 26 23:56:12 – Jun 26 23:58:46	0.15	0.3–10 keV (photon counting)
Swift/XRT	00033012215	Jun 27 00:04:44 – Jun 27 00:21:47	1.0	0.3–10 keV (photon counting)
Swift/UVOT	00033012214	Jun 26 22:19:35 – Jun 26 22:39:47	1.2	UVM2 (Event+Imaging)
Swift/UVOT	00033012213	Jun 26 23:56:12 – Jun 26 23:58:46	0.15	UVM2 (Event+Imaging)
Swift/UVOT	00033012215	Jun 27 00:04:44 – Jun 27 00:21:47	1.0	UVM2 (Event+Imaging)
VLT/FORS2	107.22RK.001	Jun 26 22:51:56 – Jun 27 01:15:30	8.7	*R*
REM/ROSS2	43013	Jun 26 23:20:33 – Jun 27 01:24:41	7.4	*griz*
REM/REMIR	43013	Jun 26 23:20:44 – Jun 27 01:25:34	7.4	*K*
ALMA	2019.A.00036.S	Jun 26 21:58:42 – Jun 27 01:12:06	9.3	Band 3 (C43-7 configuration)

2.3. HST (Night 1)

The Space Telescope Imaging Spectrograph (STIS; Woodgate et al. 1998) on board *HST* observed J1023 for 4750 s using the near UV Multi-Anode Micro-channel Array detector (NUV-MAMA) in TIME-TAG mode (time resolution of 125 µs); the data were collected with the G230L grating equipped with a 52″ × 0.2 slit with a spectral resolution of ~500 over the nominal range (first order). The data analysis procedure that we adopted is the same as that described by Miraval Zanon et al. (2022). In summary, we used the `stis_photons` package[3] to correct the position of the slit channels and to assign the wavelengths to each time of arrival (ToA). We selected ToAs belonging to channels 993–1005 of the slit and in the 165–310 nm wavelength interval to isolate the source signal.

2.4. NTT/SOFI (Night 1)

We collected NIR high time-resolution imaging data using the SOFI (Moorwood et al. 1998) instrument mounted on the European Southern Observatory (ESO) 3.6-m NTT at La Silla Observatory (Chile). Observations were carried out using the *J* filter from 2021 June 3 at 23:49:09 UTC to June 4 at 02:42:38 UTC (Table 1). In order to achieve 1-s time resolution, observations were performed in Fast Photometry mode, which restricts the area on which the detector is read. Specifically, the instrument was set to read a 400×400 pixels window (1.9′ × 1.9′). During the observation, a series of 100 frames each with an exposure time of 1.0 s were stacked together to form a "data-cube". There was a gap of ~3 s between each cube. Photometric data were

extracted through aperture photometry with an aperture radius of 1.4″ using a custom pipeline based on the DAOPHOT package (Stetson 1987b). In order to minimise systematic errors, we performed photometry on J1023 and a reference star (at position R.A. = $10^h23^m50^s54$, Dec. = +00°38′16.″4, J2000.0, and with a magnitude of $J = 15.44 \pm 0.05$ mag in the Vega system from the Two Micron All-Sky Survey (2MASS) point source catalogue), assumed to have constant brightness. We then re-binned the light curve at a time resolution of 10 s to reduce the scatter and investigate the presence of variability at the same time resolution as the light curves in the X-ray and UV bands. For a more conservative approach, we evaluated the errors on the magnitudes of the re-binned light curves as the standard deviation of the magnitudes measured in each bin.

2.5. VLA (Night 1)

The VLA observed J1023 for 4 hours, starting on 2021 June 3 at 22:30 UTC. The array was in its C-configuration and data were taken at a central frequency of 10 GHz, with a bandwidth of 4 GHz. J1331+3030 was used as flux and bandpass calibrator, while J1024−0052 was used as phase calibrator. The separation between the target and the phase calibrator is 0.3°. To calibrate and analyse the data we followed the prescription of Deller et al. (2015) and Bogdanov et al. (2018). Here we report the main steps. After initial calibration using the VLA pipeline within the Common Astronomy Software Application (CASA) package (version 5.1.1), manual flagging of bad data was performed. Unfortunately, the first half of the observation turned out to be unusable, possibly due to the bad weather conditions that occurred during the observation, and was completely flagged out.

---

[3] https://github.com/Alymantara/stis_photons

Subsequently, we self-calibrated the data using a solution interval of 75 s for the phase calibration and 45 min for the amplitude+phase calibration. Upon inspection of the field of view, three main sources were identified: the target J1023, a faint source to the north, namely J102348.2+004017, and the brightest source in the field, located to the south-east, i.e. J102358.2+003826. J102358.2+003826 is a well-known galaxy at redshift $z = 0.449$ (Ahn et al. 2014) with a resolved extended emission whose secondary lobes heavily affect the overall rms noise level (Deller et al. 2015). To remove the problematic contribution of J102358.2+003826, we first cleaned the image using a mask with the `tclean` task. We set the `nterms` parameter equal to 2 to take into account the spectral properties of the galaxy over the wide bandwidth of the observation (Deller et al. 2015). This step provided the model visibilities of J102358.2+003826. Next, we used the `uvsub` task to subtract these model visibilities from the self-calibrated visibilities and deconvolved the residuals. The resulting image therefore does not have any contribution from J102358.2+003826.

As pointed out by Deller et al. (2015), the gain solutions from the self-calibration obtained before the subtraction of J102358.2+003826 were dominated by the pointing errors of this source. This source was located beyond the half-power point of the antenna, resulting in inaccurate solutions. Therefore, we had to invert the amplitude and phase self-calibration after subtracting this source from the field. We used the CASA task `invgain` (Hales 2016) to invert the calibration table and applied it to the self-calibrated visibilities. The final image obtained had a beamwidth size of 3.6″×2.1″, and an rms noise level of $\simeq 4\,\mu$Jy beam^{-1}.

To extract the light curve, we imaged the field using a 60-s time interval and a mask around the target with the CASA `tclean` task, setting `niters=10` and `cycleniter=10`. We selected these values after evaluating random images where the target was either detected or not detected, and ensuring that this choice did not result in false positive detections. Then, we used the `imfit` task to obtain the peak flux density of the target and the check source, J102348.2+004017, for each 60-s image to investigate possible systematic effects. To measure the rms noise level around J1023 and check source, we placed four boxes around each source and used the `imstat` task to average the rms noise level within each box. To build the light curve, we considered a source as detected whenever the flux density value obtained with `imfit` was $\geq 3\sigma$; otherwise, we took 3 times the rms noise level as an upper limit. To take into account possible systematics affecting the field of view, we investigated possible correlations between the light curves of the target and the check source. No evidence of such correlations was found. Finally, we further flagged bad 60-s images and removed intervals with odd results, such as sudden increases in the flux density of J102348.2+004017.

2.6. FAST (Night 1)

FAST (Jiang et al. 2019, 2020; Qian et al. 2020) observed J1023 starting on 2021 June 4 at 08:47:45 UTC. The total integration time was 3 hr (the first two minutes and the last two minutes were dedicated to the injection of an electronic noise signal, referred to as a CAL). The observation covered a range of orbital phases from approximately 0.5 to 1.1, thus encompassing the epoch of passage of the pulsar at the inferior conjunction of the orbit. The observation sampled a total of 21 low mode episodes according to the simultaneous *XMM-Newton* observation (see Fig. 1). The central frequency was 1.25 GHz, with a range from 1.05 GHz

to 1.45 GHz, including a 20 MHz band edge on each side. The average system temperature was 25 K. The recorded FAST data stream for pulsar observations is a time series of total power per frequency channel, stored in PSRFITS format (Hotan et al. 2004) from a ROACH-2-based backend[4], which produces 8-bit sampled data over 4k frequency channels at a cadence of 49.152 μs.

We searched for pulsations with either a dispersion signature or instrumental saturation in all data collected during the observation. We performed four different types of data processing:

(i) Data folding based on the ephemeris derived from the X-ray data: we analysed the data using the ephemeris derived from the strictly simultaneous X-ray data collected by *XMM-Newton* (Miraval Zanon et al. 2022). We separately folded the FAST data from the entire observation and those obtained by stacking the data acquired during all the periods of high X-ray mode and all the periods of low X-ray mode. However, no radio pulses were detected with SNR>6 in either case.

(ii) Dedicated search for persistent periodic radio pulses: for the sake of robustness, we created de-dispersed time series for each pseudo-pointing over a Dispersion Measure (DM) range between 3 pc cm^{-3} and 100 pc cm^{-3}. This range covers all uncertainties of the semi-blind search, as J1023 was discovered at a DM of 14.3 pc cm^{-3} (Archibald et al. 2009). We set the step size between subsequent trial DMs equal to the intra-channel smearing over the entire band. This ensures that any trial DM deviating from the source DM by ΔDM will not cause extra-smearing beyond the intra-channel smearing. We used the PulsaR Exploration and Search TOolkit pipeline (PRESTO; Ransom 2001) to search for periodic signals in the power spectrum for each trial DM. We allowed the power of the highest harmonic component of the signal to drift in the Fourier domain up to a maximum number of 200 frequency bins and 50 frequency derivative bins (jerk search; Andersen & Ransom 2018; see also Wang et al. 2021). This corresponds to an acceleration of 90.93 m s^{-2} and a jerk of 0.002 m s^{-3} for the fundamental component. After checking all signal candidates with SNR>5, we identified them as narrow-band radio frequency interference (RFI).

(iii) Search for single pulses: we used the dedicated search scheme in (ii) to de-disperse the data. We then applied 14 box-car width-match filter grids distributed in logarithmic space from 0.1 to 30 ms. A zero-DM matched filter was used to mitigate RFI in the blind search. All the resulting candidate plots were visually inspected, but most were determined to be RFI. No pulsed radio emission with a dispersive signature was detected with SNR>5.

(iv) Search for baseline saturation: we acknowledge that FAST would become saturated if the radio flux density reached levels as high as kJy to MJy. Therefore, we also searched for saturation signals in the recorded data-set. We looked for epochs where at least half of the channels satisfied one of the following conditions: 1) the channel was saturated (255 value in 8-bit channels), 2) the channel had a zero value, or 3) the rms deviation of the bandpass was <2. We did not find any instances of saturation lasting >0.5 s during the observational campaign.

We then calibrated the noise level of the baseline with noise CAL injection, and derived a 5-σ flux density upper limit for persistent radio pulsations of 2.0±0.5 μJy at 1.25 GHz considering the entire integration time of 2.8 hr, assuming a pulse duty cycle between 0.05–0.3 (which is typical for MSPs; see the ATNF pulsar catalogue; Manchester et al. 2005) and disregarding the possible scintillation effect. Within the uncertainty of the flux measurements and stability threshold, no flux variations were

---

[4] https://casper.astro.berkeley.edu/wiki/ROACH-2_Revision_2

seen during the observation, consistent with an apparent lack of scintillation. The 5-σ flux upper limits on the pulsed flux density of J1023 during the high and low modes can be evaluated by scaling the above-mentioned limit for the specific integration time-spans during the high and low-mode periods in the X-rays: we obtain upper limits of $2.2\pm0.6\,\mu$Jy in the high mode (2.3 hr) and $4.7\pm1.0\,\mu$Jy in the low mode (0.5 hr).

2.7. NICER/XTI observations (Night 2)

The X-ray Timing Instrument (XTI) mounted on *NICER* (Gendreau et al. 2012) observed J1023 between 2021 June 26 at 21:56:04 UTC and 2021 June 27 at 01:33:51 UTC, for an exposure time of ~6.1 ks. The raw, unfiltered data were processed and analysed using tools within the NICERDAS software package and the latest version of the calibration files at the time of the analysis (CALDB v. 20221001)[5]. We extracted the background-subtracted light curve in the 0.5–10 keV energy range with a time bin of 10 s using the NICERL3-LC high-level pipeline, which estimates the background level using the "Space Weather" background model.

2.8. Swift/XRT observations (Nights 1 and 2)

The *Swift* (Gehrels et al. 2004) X-ray Telescope (XRT; Burrows et al. 2005) observed J1023 in the photon-counting mode (time resolution of 2.5 s) both during Night 1 and Night 2. The first observation started on 2021 June 3 at 18:29:46 UTC and consisted of 11 snapshots, with a total elapsed time of $\simeq$51.3 ks and an effective exposure time of ~17.9 ks. The second observation started on 2021 June 26 at 22:19:35 UTC and consisted of three snapshots, resulting in a total elapsed time of $\simeq$7.3 ks and an effective exposure time of ~2.4 ks. The raw, level-1 data were processed and screened using standard criteria. Source photons were collected from a circular aperture of radius 47.2″ centred on J1023 and background photons were collected from an annular region with inner and outer radii of 94.4″ and 188.8″, respectively, also centred on J1023. We extracted a background-subtracted time series with a time bin of 100 s, suitable to sample adequately the X-ray mode switching (see Figs. 1 and 3).

2.9. Swift/UVOT observations (Nights 1 and 2)

The *Swift* Ultra-Violet/Optical Telescope (UVOT; Roming et al. 2005) observed J1023 simultaneously with the XRT. The observations were performed in both image and event modes using the UVM2 filter (central wavelength 2260 Å; full-width at half-maximum 527 Å). Data were processed and analysed in the standard way. For the source photons, we used a circular extraction region of radius of 5″ centred on the source position. For the background photons, we adopted a circular extraction region of radius 20″ away from source. For the data in image mode, photometry was carried out using the UVOTSOURCE task. For the data in event mode (time resolution of 11 ms), we used the COORDINATOR tool to convert raw coordinates to detector and sky coordinates, UVOTSCREEN to filter out hot CCD pixels and obtain a cleaned event list, and UVOTEVTLC to extract a background-subtracted light curve with a time bin of 120 s, which provided a sufficiently high SNR to detect any changes in the UV brightness at least during the longest periods of low X-ray mode.

2.10. REM photometric observations (Night 2)

We observed J1023 during Night 2 with the 60-cm REM telescope (Zerbi et al. 2001; Covino et al. 2004) located at La Silla Observatory (Chile). We obtained 48 strictly simultaneous exposures with the ROSS2 imager, each with an integration time of 60 s, with SDSS *griz* optical filters (Table 1). We reduced the images following standard procedures (bias subtraction and division by a normalized flat-field), and performed aperture photometry with the PHOT tool in IRAF using an aperture size of 6 pixels. We performed flux calibration using stars in the field from the American Association of Variable Star Observers (AAVSO) Photometric All-Sky Survey (APASS) catalogue[6] (Henden 2019). We obtained simultaneous *K*-band observations with the REMIR instrument. A total of 300 15-s integration images were acquired, which we combined 5 by 5 to correct for the background contribution. Aperture photometry was performed with IRAF as described above. The images were flux-calibrated against a selection of stars in the field from the 2MASS point source catalogue[7].

2.11. VLT/FORS2 polarimetric observations (Night 2)

We observed J1023 with the FOcal Reducer/low dispersion Spectrograph 2 (FORS2; Appenzeller et al. 1998) mounted on the 8.2-m VLT at Paranal Observatory (Chile) in polarimetric mode using the optical filter *R_SPECIAL* + 76 (*R*; central wavelength 655 nm, full-width-half-maximum 165 nm) during Night 2. The observations were performed under thin cirrus clouds conditions, with seeing varying from 0.4″ to 0.9″. A total of 156 short (10 s) exposures were taken, resulting in a total observing time of ~2.41 hr on source, overheads included (~50% of the 4.75 hr orbital period).

A Wollaston prism was inserted in the optical light path to split the incident radiation into two orthogonally polarised light beams called ordinary (*o*-) and extraordinary (*e*-) beams. A Wollaston mask was introduced to avoid overlap of the beams on the CCD. In addition, a rotating half-wave plate (HWP) was inserted, allowing images to be taken at four different angles (Φ_i) of the plate with respect to the telescope axis: $\Phi_i = 22.5°(i - 1)$, $i = 1, 2, 3, 4$. This step is essential to obtain a polarisation measurement, since the set of images at the four different angles must be combined to evaluate the level of linear polarisation (as described below). Therefore, a total of 39 polarisation epochs were acquired with the program. All images were processed by subtracting an average bias frame and dividing by a normalized flat field. Aperture photometry was performed using the DAOPHOT tool (Stetson 1987a), using an aperture of 6 pixels. The normalised Stokes parameters *Q* and *U* for the linear polarisation (LP) were evaluated following the methods described by Baglio et al. (2020) and references therein. These values were then corrected for instrumental polarisation by observing a non-polarised standard star[8] (WD 1620-391) using the same setup during the same night. A polarisation level of < 0.2% was measured, which is consistent with the typical instrumental polarisation level expected for the FORS2 instrument as reported on the ESO website[9] (<0.3% in all optical bands). The Stokes pa-

---

[5] We followed the standard procedures outlined on the NICER data analysis webpage (https://heasarc.gsfc.nasa.gov/docs/nicer/analysis_threads/).

[6] http://www.aavso.org/download-apass-data

[7] https://irsa.ipac.caltech.edu/applications/2MASS/IM/

[8] https://www.eso.org/sci/facilities/paranal/instruments/fors/tools/FORS1_Std.html

[9] http://www.eso.org/observing/dfo/quality/FORS2/reports/FULL/trend_report_PMOS_inst_pol_FULL.html

rameters evaluated for the non-polarised standard star were then subtracted from the Stokes parameters of J1023 at each epoch.

We then used an algorithm to estimate the level and angle of linear polarisation. This algorithm is based on the evaluation of the quantity $S(\Phi)$ for each of the HWP angles (e.g. di Serego Alighieri 1998 and references therein; see also Covino et al. 1999; Baglio et al. 2020). $S(\Phi)$ is the component of the Stokes vector that describes the LP along the Φ direction (e.g., $S(0°) = Q$). It is defined as:

$$S(\Phi) = \left(\frac{f^o(\Phi)/f^e(\Phi)}{f^o_u(\Phi)/f^e_u(\Phi)} - 1 \right) \left(\frac{f^o(\Phi)/f^e(\Phi)}{f^o_u(\Phi)/f^e_u(\Phi)} + 1 \right)^{-1}, \qquad (1)$$

where Φ is the angle of the HWP, $f^o(\Phi)$ and $f^e(\Phi)$ are the ordinary and extraordinary fluxes for a given angle Φ, and $f^o_u(\Phi)$ and $f^e_u(\Phi)$ are the same quantities evaluated for the non-polarised standard star. $S(\Phi)$ is related to the polarisation level P and angle θ by $S(\Phi) = P \cos 2(\theta - \Phi)$. The parameters P and θ were estimated by maximizing the Gaussian likelihood function and using this as the starting point for a Markov Chain Monte Carlo (MCMC) procedure (Hogg & Foreman-Mackey 2018) (see Baglio et al. 2020 for further details on the algorithm). The best fit parameters were then calculated as the median of the marginal posterior distributions of these parameters, while the uncertainties were estimated as the 16–84th percentiles of the distributions. For non-detections, the 99.97% percentile of the posterior distribution of the parameter P was used to calculate an upper limit.

After fitting the $S(\Phi)$ curve, we obtained an LP value that is already corrected for instrumental effects. However, the polarisation angle still needs to be corrected using the Stokes parameters of a polarised standard star. For this purpose, we observed the star Hiltner 652 and measured its Stokes parameters to determine its polarisation angle. This was then compared to the tabulated value, and a difference of $1.71° \pm 0.30°$ was applied to the polarisation angle of J1023. However, the resulting linear polarisation will still include an interstellar component. Evaluating the interstellar contribution is not straightforward. In principle, we could use a group of reference stars in the same field as the target in Eq. 1, under the assumption that these stars are non-polarised. This way, the LP of the target would be corrected for both instrumental and interstellar contributions. However, it is important to ensure that the chosen reference stars all have the same level of polarisation, which would be a good indication of their intrinsic non-polarised nature (see e.g. Baglio et al. 2020). Unfortunately, not only is the field of view of J1023 sparse in the optical, but the very short exposure times (10 s) exclude all faint ($R > 19$) stars from this study. We are therefore left with only one possible comparison star in the field, which makes it difficult to verify whether the chosen star is indeed intrinsically non-polarised. As a result, we used the fluxes of the non-polarised standard star in Eq. 1. The field star will be used as a comparison for the analysis.

We can evaluate the maximum interstellar contribution to the LP of a source, referred to as P_{int}, through considerations of its absorption coefficient in the V-band, A_V: $P_{int}(\%) < 3A_V$ (Serkowski et al. 1975). For J1023, the best-fitting absorption column density, N_H, according to *XMM-Newton* observations is $5.0^{+0.3}_{-0.2} \times 10^{20}$ cm^{-2} (Campana et al. 2019). Using the relation between N_H and A_V in our Galaxy from Foight et al. (2016), we calculate $A_V = 0.17 \pm 0.01$ mag and therefore $P_{int} < 0.52\%$. This is very low and comparable to the instrumental polarisation measured for the instrument configuration. It is also comparable to the upper limit of the interstellar polarisation measured for J1023 (Baglio et al. 2016).

Table 2. ALMA continuum maps

Weighting	Synthesized beam ($'' \times ''$)	P.A (°)	rms[a] (μJy beam^{-1})
Natural	0.87×0.53	−74.5	6.1
Briggs, `robust=0`	0.55×0.30	−87.3	10.6

[a] Rms noise level at the phase center.

2.12. ALMA observations (Night 2)

The ALMA observations were conducted using the 12 m array and 38 antennas in the C43-7 configuration (baselines 22–2492 m), with a field of view (FoV) of 59.72′′ and a maximum recoverable scale of 11.5′′. The total integration time on source was ~2 hr and the phase center was R.A. = $10^h23^m47^s68$; Dec. = $+00°38'41.''00$ (ICRS). The weather conditions were good and stable, with an average precipitable water vapor of ~1.2 mm and an average system temperature of $\simeq$65 K. The band-pass and flux calibrators used were J1058+0133 and J1256−0547, while J1028−0236 was used as the phase calibrator. The continuum image was obtained by averaging the four base-bands of width 1.875 GHz, each centered at 90.5003 GHz, 92.5003 GHz, 102.5003 GHz, and 104.5003 GHz, covering a total bandwidth of 7.5 GHz. No spectral lines were detected within the observed frequency range above the 3σ noise level per spectral channel of ~0.48 mJy beam^{-1}.

Data reduction was carried out following standard procedures using the ALMA pipeline within CASA (v. 6.1.1-15)[10]. Continuum images were produced using TCLEAN interactively and applying a manually selected mask. These images were corrected for primary beam attenuation and were produced using both natural weighting and a Briggs `robust=0` weighting (Briggs 1995). The former maximises the sensitivity whereas the latter provides higher angular resolution. The mean frequency of the continuum image is 97.51 GHz, which corresponds to a wavelength of 3.1 mm. Table 2 lists the synthesized beam and the root mean square (rms) noise of each image.

3. Results

3.1. X-ray and UV emissions

The X-ray light curve extracted from *XMM-Newton* data during the first night reveals flaring activity over a time span of ~1.5 hr at the beginning of the observation. A total of 288 switchings between high and low modes were observed during the observation (see Fig. 1). Based on our thresholds for the EPIC net count rates in the different modes (see Miraval Zanon et al. 2022), we estimated that J1023 spent $\simeq$65, 17 and 1% of the time in the high, low and flaring modes, respectively, and the rest of the time switching between modes. The good time intervals (GTIs) corresponding to the high and low modes were then used to extract the background-subtracted spectra, response matrices, and ancillary files separately for each mode. The *NuSTAR* light curve is characterised by a lower SNR than the *XMM-Newton*/EPIC light curve. Nevertheless, it is possible to recognise the same flaring episodes and mode switchings detected using *XMM-Newton* (see Fig. 1). We used the GTIs for the high and low modes selected by the strictly simultaneous *XMM-Newton*/EPIC light curves to extract the background-subtracted spectra, response matrices, and ancillary files separately for each mode.

The X-ray light light curve extracted from NICER data during the second night, shown in the top panel of Fig. 3, re-

---

[10] https://casa.nrao.edu

veals 22 instances of X-ray mode switching, without any obvious flaring episodes. We applied intensity thresholds to the light curve to select the time intervals corresponding to the high (>2.5 counts s^{-1}) and low (<2.5 counts s^{-1}) X-ray modes. Based on this selection, we estimate that J1023 spent ~70% of the time in the high mode and ~30% of the time in the low mode. We also detected two periods of X-ray low mode in the *Swift*/XRT data, with the former also covered by the *NICER* observations (see the second panel of Fig. 3).

The UV light curves exhibit substantial variability. Specifically, the HST light curve during Night 1 displays flaring activity as well as dips in the count rate that coincide with the low-mode episodes observed in X-rays (Fig. 1; see also Miraval Zanon et al. 2022; Jaodand et al. 2021). A dip in the UV brightness by ~0.7 mag is also clearly visible in the *Swift*/UVOT data during the third snapshot of Night 2. The decrease occurs over a span of several minutes during an episode of low mode (Fig. 3).

3.2. Optical/NIR photometric properties

During the first night, the source is brighter at the beginning than in the rest of the observation (reaching $B \simeq 17 - 16.5$ mag), displaying a smooth quasi-sinusoidal modulation at the orbital period with a semi-amplitude of $\simeq 0.2$ mag around an average value of $B \simeq 17.3$ mag. We fit a sinusoidal function to the light curve by fixing the period and reference phase of the sinusoid to the binary orbital period and the phase value obtained from the time of passage of the pulsar through the ascending node, respectively, as derived by Miraval Zanon et al. (2022). Then, we subtracted the best-fitting function from the observed count rates. The resulting detrended light curve is shown in Fig. 1. After initial flaring activity resembling the X-ray behaviour, the optical intensity appears to be flickering, but without any sign of mode switching.

Fig. 1 also shows the NIR light curve. Variability in the form of dips and flickering is evident. The fractional rms magnitude deviation of the light curve, computed following the method described by Vaughan et al. (2003), is (10.1±0.2)%. No NIR flare was observed at the switch from the low to the high X-ray mode, as previously reported (Papitto et al. 2019; Baglio et al. 2019). Furthermore, we did not detect any signs of mode switching in the light curve. The average magnitudes measured separately during the high and low modes are compatible within 1σ ($J = 15.39 \pm 0.16$ mag and $J = 15.37 \pm 0.13$ mag in the high and low modes, respectively), indicating that there is no significant correlation between the NIR variability and mode switching.

During Night 2, the optical light curves show clear variability on short timescales (Fig. 3, fourth panel). Unlike what was seen during Night 1, no modulation at the system orbital period is detected. The average magnitudes are $g = 16.65 \pm 0.02$ mag, $r = 16.45\pm0.02$ mag, $i = 16.20\pm0.03$ mag, $z = 16.09\pm0.03$ mag (in the AB photometric system), all marginally consistent with those reported by Coti Zelati et al. (2014); Baglio et al. (2016). To estimate the amount of intrinsic variability, we evaluated the fractional rms magnitude deviation of the light curves following Vaughan et al. (1994). We find a low-significance fractional rms of $6.2 \pm 3.4\%$, $6.9 \pm 2.3\%$ and $12.7 \pm 4.7\%$ at a time resolution of 160 s in the g, r and z bands, respectively, while no excess intrinsic variability could be detected in the i band. This fractional rms is comparable to what has been observed for a few black-hole X-ray binaries in the optical band on a similar timescale, such as GX 339-4 (Gandhi 2009; Gandhi et al. 2010) and MAXI J1535−571 (Baglio et al. 2018). In these systems, the variability has been attributed to the emission of a flickering jet that contributes up to optical frequencies. In contrast, when accretion dominates, lower values of fractional rms are typically measured, as seen in the case of the black-hole X-ray binary GRS 1716−249 (Saikia et al. 2022).

Unfortunately, most of the K-band images are of bad quality, resulting in an empty field of view. We stacked together three of the combined images in which the field was visible and J1023 was detected (so a total of 15×15 s integration images, all taken during the high mode), and performed the calibration against a selection of stars in the field from the 2MASS point source catalogue. We obtained an average magnitude of $K = 14.41 \pm 0.29$ mag, which is consistent with previous values reported in the literature (see e.g. Coti Zelati et al. 2014; Baglio et al. 2016).

3.3. Optical polarimetric properties

Fig. 3 shows the evolution of the optical LP level during the second night of observations. To improve the SNR of the observations without losing too much information on the short-term variability of the LP, we combined the measurements so that each LP data point covers 80 s (4 HWP angles × 10 s of integration × 2 sets). We define an LP measurement as a detection when it reaches a confidence level of greater than 2σ. Using this threshold, we obtain a total of 8 LP detections and 11 upper limits at a 99.97% confidence level (see Table 3). The average level of linear polarisation, calculated as the average of all 2σ-significant detections, is $0.92 \pm 0.39\%$. This is consistent with previous results in the same band (R-band; Baglio et al. 2016). The polarisation angle is well constrained at a value of $(6^{+18}_{-15})°$ (corrected for the polarisation angle of the standard star).

When detected, the LP appears fairly constant throughout the observations. We investigated any potential changes in the LP level as a function of the X-ray mode (low/high) by averaging all images taken during the high and low modes. We found that the LP was $0.65 \pm 0.43\%$ (with a 99.97% confidence level upper limit of 2.12%) in the high mode and $0.36^{+0.27}_{-0.35}\%$ (with a 99.97% confidence level upper limit of 1.58%) in the low mode.

The measured levels of LP are not corrected for interstellar contribution, which is expected to be low according to Serkowski's law (<0.52%; Serkowski et al. 1975). Fig. 5 shows the Q and U Stokes parameters on the $Q - U$ plane for the whole dataset, including J1023 (black dots), a comparison star in the field (red squares), and the non-polarised standard star (green star). The non-polarised standard star is located very close to the origin of the $Q - U$ plane, indicating that the instrumental polarisation of VLT/FORS2 is low, as expected. The Stokes parameters of the comparison star, on the other hand, are scattered around a common point, consistent with the position of the non-polarised standard within ~1.5δ, where δ is the standard deviation of the points. Any deviation from the position of the non-polarised standard on the plane is a good estimate of the interstellar polarisation of the field (assuming that the comparison star is intrinsically non-polarised). Interestingly, the Stokes parameters of J1023 are clustered around a common point in a different region of the $Q - U$ plane, with a higher scatter than the comparison star due to larger uncertainties. For the two time-series of the Q and U Stokes parameters, we are unable to claim any detection of short-timescale variability.

3.4. Millimetre emission

Fig. 6 shows the ALMA 3.1 mm continuum emission towards J1023. Two sources were detected within the FoV of ALMA.
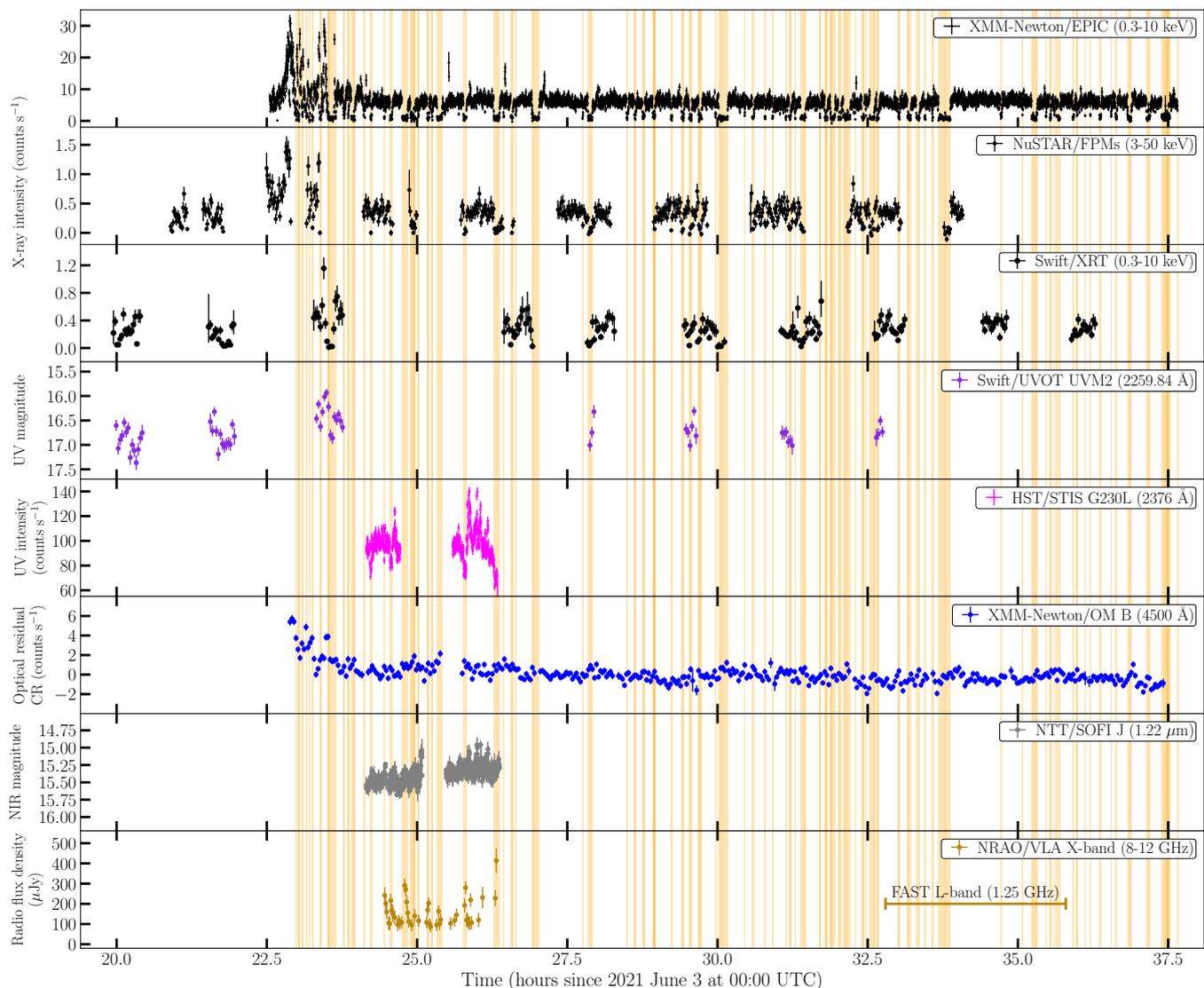
Fig. 1. Temporal evolution of the X-ray, UV, optical, NIR and radio emissions of J1023 on 2021 June 3–4. The light curves are shown in decreasing order of energy band from top to bottom with the *XMM-Newton*/EPIC one as the reference for all others (*NuSTAR*, *HST*/STIS, *XMM-Newton*/OM, NTT/SOFI, VLA). The *XMM-Newton* X-ray light curve is shown over the time interval in which the three EPIC instruments collected data simultaneously. The OM residual count rates were obtained after removing the orbital modulation from the time series (see the text for details). Only VLA detections are shown for displaying purpose. The dark yellow segment in the bottom panel indicates the time range covered by the FAST observation. The orange shaded areas mark the time intervals of the low X-ray mode detected by *XMM-Newton*/EPIC covered by observations with other instruments.

J1023 was detected at a significance level of ∼15σ. The other source, which we designate ALMA J102349.1+003824 following the naming convention of new sources discovered by ALMA, is located ∼22″ south-east of J1023 and was detected at a significance level of ∼9σ. The panels on the right of the figure display the zoom-in maps around each source, with the continuum image obtained with natural weighting displayed in color scale and the black contours derived from the image with `robust=0`. Table 4 reports the peak coordinates, the peak intensity, the integrated flux, and the deconvolved size obtained by fitting a two-dimensional Gaussian function to the high-resolution image (`robust=0`).

The 3.1-mm continuum emission from J1023 has a compact shape with some elongation towards the southeast (shown in the top right panel of Fig. 6 using black contours). The millimetre continuum emission peaks ∼0.32″ south of the optical position. The deconvolved size obtained from the 2D Gaussian fit in the `robust=0` image is 0.305″ × 0.205″, which corresponds to approximately 418AU × 281AU (∼6.3×10^{15} cm × 4.2×10^{15} cm) at a distance of 1.37 kpc (this is approximately 7×10^4 times the orbital separation of the system; Archibald et al. 2013). The emission from ALMA J102349.1+003824 also appears compact (see the bottom right panel of Fig. 6). The 2D Gaussian fit yields a point-like source with a FWHM as large as 0.39″×0.22″ (see Table 4). The results of the searches for counterparts of this source at other wavelengths are reported in Appendix A.

To determine the spectral index of J1023 within the ALMA bandwidth, we imaged the continuum emission from the lower and upper sidebands, which have central frequencies of 91.47886 GHz and 103.5115 GHz, respectively. The resulting
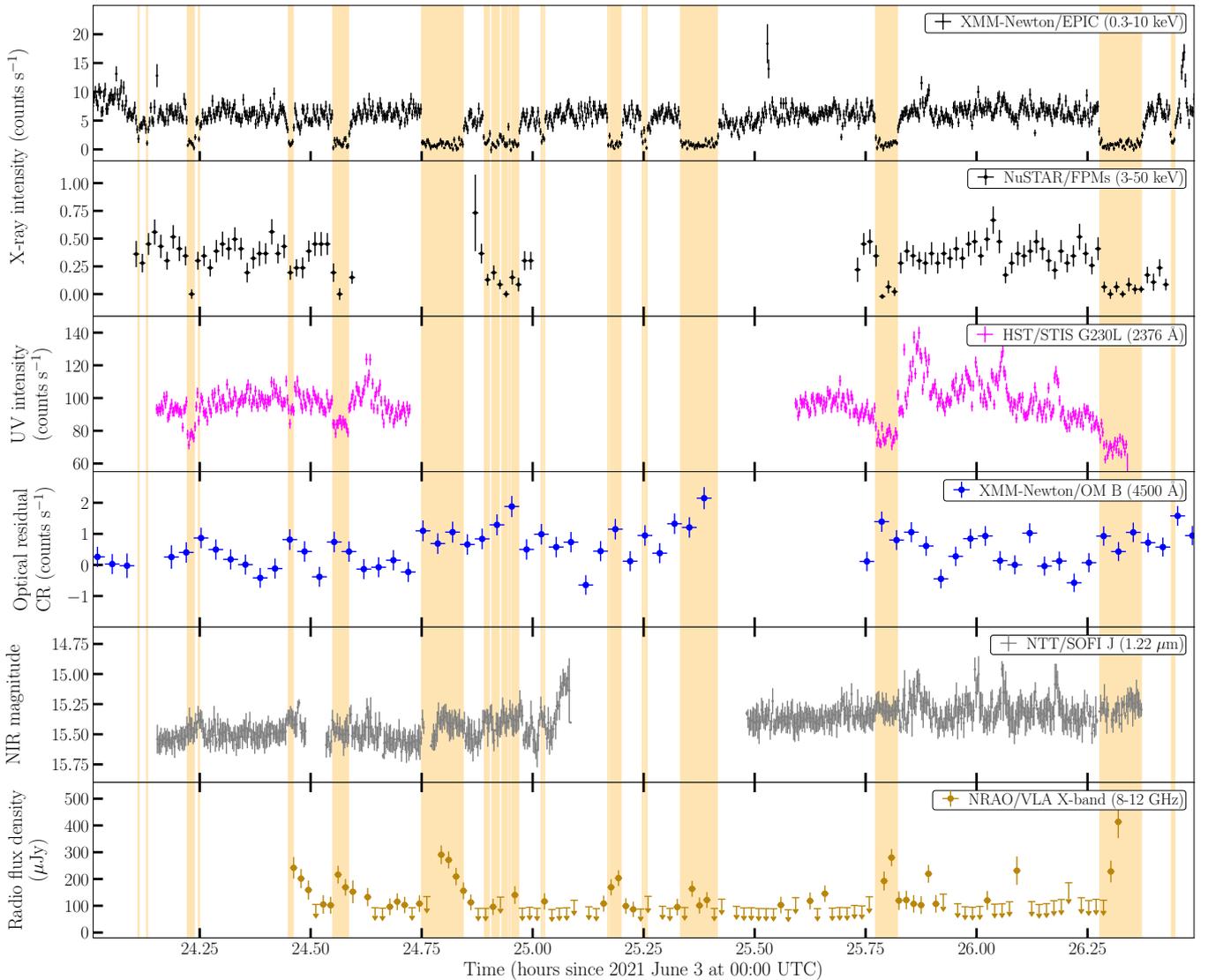
Fig. 2. Zoom-in of the time series collected on Night 1 over the time span of maximum overlap among the different telescopes. Arrows indicate 3-σ upper limits.

spectral index is -0.1 ± 0.8, which is consistent with previous reports for the average cm emission (Deller et al. 2015; Bogdanov et al. 2018).

To probe variability in the millimetre emission, we obtained images scan by scan (typically with a duration of ~4–5 minutes), using a natural weighting. We then computed the peak intensities and flux densities considering the emission above 3σ level. The bottom panel of Fig. 3 shows the evolution of the flux density over time. This quantity was found to vary by a factor of ~5 within the range ~30–160 μJy on a timescale of about 5 minutes. In some cases, the flux density remained below the detection sensitivity, resulting in upper limits of the order of a few tens μJy. Fig. 3 also shows the ALMA time series extracted using time intervals of variable length corresponding to the durations of the X-ray-mode episodes. Two flaring episodes can be clearly seen. We measured average flux densities of 89 ± 13 μJy in the high mode and 134 ± 23 μJy in the low mode, excluding the two flaring episodes (see Table 5). Overall, the anticorrelated variability

pattern appears to be more pronounced between the cm and X-ray emission than between the millimetre and X-ray emissions.

3.4.1. Millimetre flares

The integration times adopted above are effective for studying the variability of the millimetre emission on minute timescales, but may average out large enhancements of the millimetre flux on much shorter timescales (of the order of seconds). Therefore, we performed a dedicated search for short flaring episodes by extracting images of different durations using the entire dataset. This search resulted in the detection of the two above-mentioned episodes of bright millimetre emission (Fig. 4). No other remarkable events were detected. The first episode (hereafter "Flare 1") occurred on 2021 June 26 within the time range 22:19:29 – 22:19:44 (UTC) at the switch from high mode to low mode and reached a peak flux density of 1.01 ± 0.08 mJy. The second event ("Flare 2") took place during the time range 23:48:29 – 23:48:44 (UTC) and reached a peak flux density of 0.7 ± 0.1 mJy.
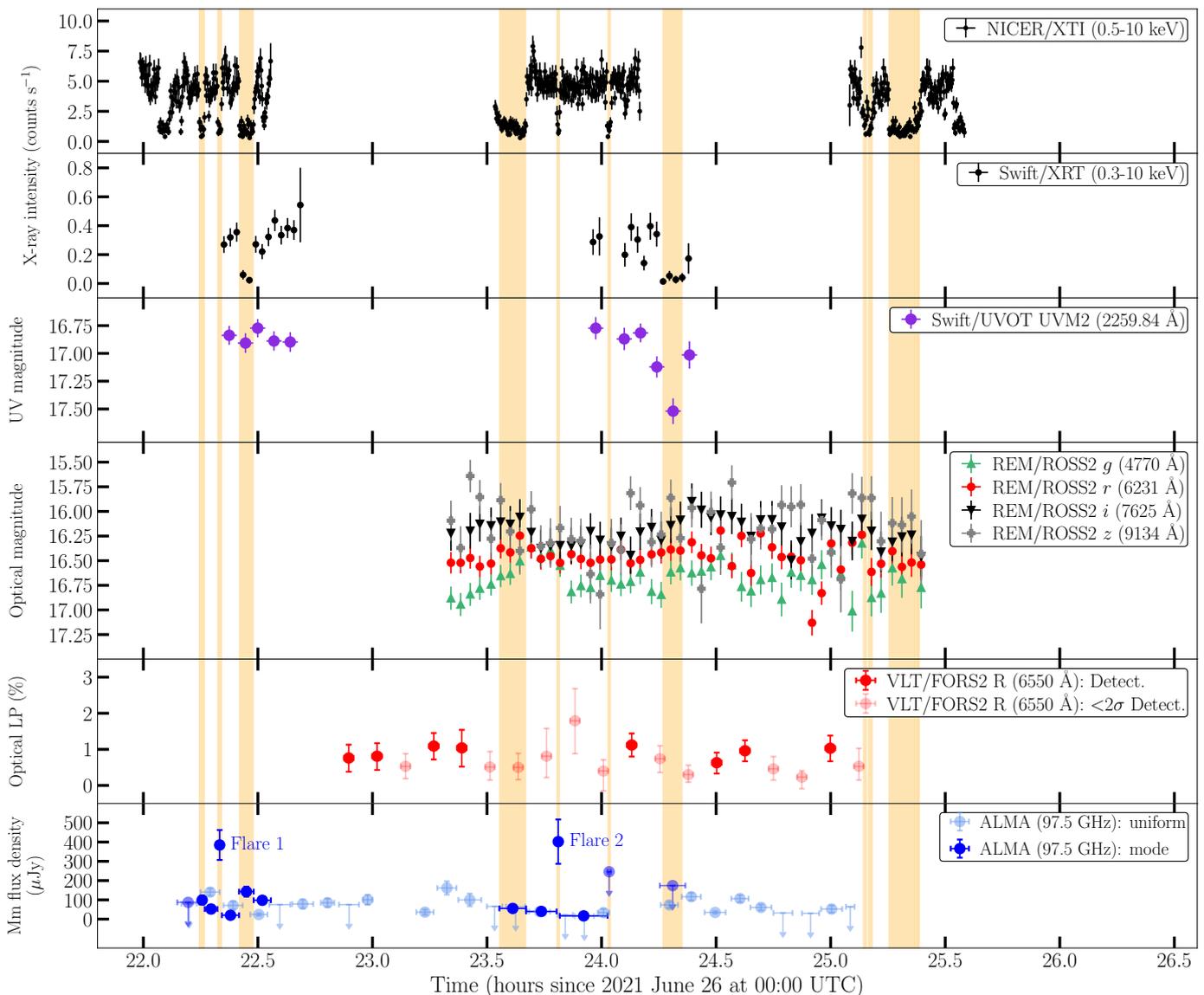
Fig. 3. Temporal evolution of the X-ray, UV, optical and millimetre emissions and of the optical linear polarisation of J1023 on 2021 June 26–27. The light curves are shown in decreasing order of energy band from top to bottom (*NICER*, *Swift*/XRT, *Swift*/UVOT, REM, VLT/FORS2 polarisation, ALMA). In the bottom panel, the ALMA time series are plotted using either bins of length 4-5 min (cyan) or bins of variable length corresponding to the duration of the X-ray mode episodes identified by the strictly simultaneous *NICER* and *Swift* data (blue). In some panels, the sizes of the markers are bigger than the uncertainties and/or the time bins. Arrows indicate 3σ upper limits. The orange shaded areas mark the time intervals of low X-ray mode detected by *NICER* and *Swift*/XRT covered by observations with other instruments. A plot of the X-ray and millimetre light curves around the epoch of the millimetre flares is shown Fig. 4.

The lack of continuous coverage in the millimetre band before and during the switch from the high to the low mode does not allow us to determine the exact epoch of the flare onset. We note that these values refer to the flux at the peak of the flares and are therefore higher than those obtained in the X-ray mode-resolved analysis (see Fig. 3 and Table 6), where the emission is averaged over longer time intervals. We observed a significant increase of the peak intensity above the average level: a factor of ~4 for Flare 1 and a factor of ~7 for Flare 2.

We observed a clear change in the morphology of the millimetre continuum emission during the two flaring episodes (see white contours in Fig. 7). The two-dimensional Gaussian fitting (see Table 6) indicates that the emission is elongated along the northeast to southwest direction during Flare 1 (roughly perpen-

dicular to the ALMA 3.1 mm emission obtained with all the visibilities), while it is marginally resolved in only one direction during Flare 2. The positional accuracy of ALMA images can be estimated as $beam_{FWHM} \times (0.9 \times SNR)^{-1}$ [11], where $beam_{FWHM}$ is the full-width-half-maximum synthesized beam in arcsec and SNR is the signal-to-noise ratio of the image. The positional accuracy for Flare 1 is $\simeq 0.12 - 0.15''$, while for Flare 2 it is slightly smaller at $\simeq 0.1''$. However, the actual absolute positional accuracy may be worse than the nominal values, potentially by a factor of two or more, depending on the atmospheric phase conditions during the observation. The offset between the ALMA peak positions and the radio position (Deller et al. 2012) is $\simeq 0.4''$

[11] https://almascience.eso.org/documents-and-tools/cycle9/alma-technical-handbook
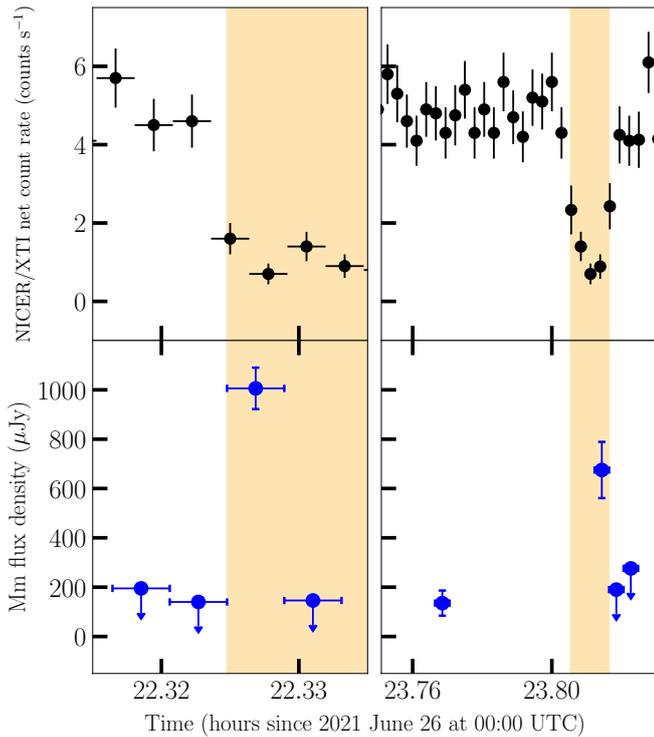
Fig. 4. X-ray (top) and millimetre (bottom) time series collected around the epochs when the two millimetre flares were detected. The X-ray light curve is binned at a time resolution of 10 s while the millimetre light curve is binned at 15 s. Arrows indicate 3-σ upper limits. Note the lack of coverage in the millimetre band for Flare 2 before and during the switch from the high to the low mode in the time interval between two consecutive ALMA scans. Note also the different scales on the horizontal axis in the panels on the left and on the right.
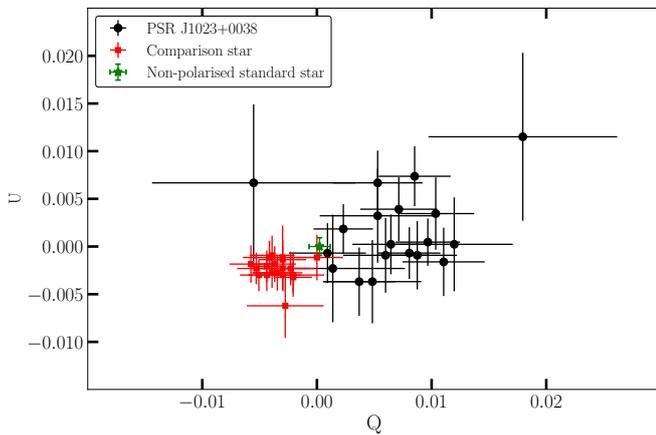
Fig. 5. Stokes Q and U measurements for the whole VLT/FORS2 dataset. Black dots, red squares and the green star indicate the Stokes parameters of J1023, a comparison star in the field and the non-polarised standard star, respectively.

for Flare 1 and ≃0.3″ for Flare 2. Given the stable weather conditions during the observation, it is possible that this offset is genuine for both flares. However, caution must be exercised, as this offset is comparable to the positional accuracy of ALMA.

Table 3. Linear polarisation detections and angles with a significance >2σ. For non-detections, upper limits are quoted at a confidence level of 99.97%. The first column indicates, in parentheses, which mode the MJD refers to ('L' for low mode, 'H' for high mode, '?' when unknown due to the lack of simultaneous X-ray observations).

Epoch (MJD)	LP (%)	PA (°)	Upper limit (%)
59391.95402 (?)	$0.76^{+0.38}_{-0.37}$	$27.32^{+15.41}_{-14.08}$	
59391.95917 (?)	$0.81^{+0.38}_{-0.36}$	$-3.57^{+13.33}_{-12.62}$	
59391.96436 (?)	–	–	1.77
59391.96949 (?)	$1.09^{+0.37}_{-0.36}$	$-2.92^{+9.28}_{-9.37}$	
59391.97459 (?)	$1.04^{+0.52}_{-0.50}$	$1.56^{+13.82}_{-14.64}$	
59391.97971 (?)	–	–	1.99
59391.98485 (L)	–	–	1.82
59391.99000 (H)	–	–	3.42
59391.99517 (H)	–	–	4.77
59392.00034 (H)	–	–	2.33
59392.00549 (H)	1.12 ± 0.32	$21.96^{+8.14}_{-8.41}$	
59392.01063 (?)	–	–	2.02
59392.01578 (?)	–	–	1.22
59392.02094 (?)	$0.63^{+0.30}_{-0.28}$	$-6.46^{+12.98}_{-12.57}$	
59392.02608 (?)	0.96 ± 0.29	$1.38^{+7.58}_{-7.56}$	
59392.03126 (?)	–	–	1.61
59392.03643 (?)	–	–	1.27
59392.04160 (?)	$1.03^{+0.36}_{-0.35}$	$9.39^{+10.11}_{-10.82}$	
59392.04680 (H)	–	–	2.25

3.5. Radio emission

3.5.1. Continuum emission

The radio light curve extracted from VLA data is shown in Fig. 1. J1023 is not detected most of the time, especially during the high mode intervals. However, it is detected during almost all episodes of low mode (here the uncertainties on the flux densities are reported at the 1σ confidence level). The average radio flux densities measured separately in the high and low mode are reported in Table 7. These values are consistent with those reported by Bogdanov et al. (2018) within the uncertainties. This indicates that the radio flux densities measured separately in the two modes are remarkably stable over time scales of years.

3.5.2. Non-detection of pulsed emission

The limit on the radio pulsed flux density derived from the FAST observations is a factor of >5000 smaller than the flux density measured at similar frequencies when J1023 was active as a radio pulsar (Archibald et al. 2009) and a factor of a few tens more constraining than the limits previously evaluated (again at similar frequencies) as soon as J1023 transitioned to the sub-luminous X-ray state (Stappers et al. 2014; Patruno et al. 2014). The limit on the radio pulsed flux density in the high mode is also at least four orders of magnitude smaller than the value predicted by extrapolating the best-fitting power-law model for the SEDs of the optical-to-X-ray pulsed emission (Papitto et al. 2019; Miraval Zanon et al. 2022).

Table 4. Parameters of the sources detected at 3.1 mm with ALMA.

Source	R.A (ICRS) (hh:mm:ss)	Dec. (ICRS) (°:′:″)	I_ν[a] (μJy beam^{-1})	S_ν[b] (μJy)	Deconvolved Size[c] (″×″)	P.A (°)
PSR J1023	10:23:47.689±0.001	00:38:40.677±0.004	103.7±3.6	144.6±8.0	(0.305±0.060)×(0.205±0.031)	86±29
ALMA J102349.1	10:23:49.131±0.002	00:38:23.72±0.02	95±15	109±29	<0.39×0.22[d]	...

[a] Peak intensity. [b] Integrated flux. [c] FWHM obtained from 2D Gaussian fits. [d] Component is a point source.
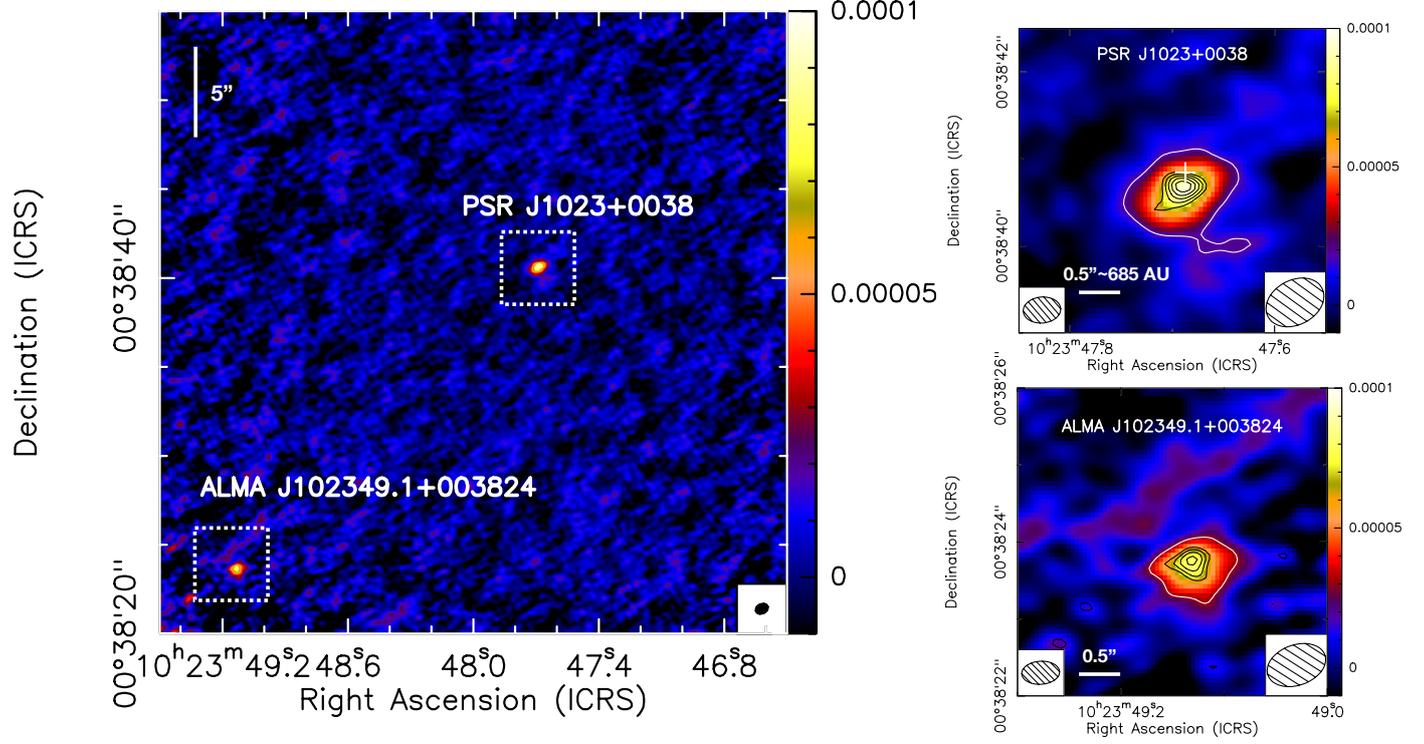
Fig. 6. *Left:* ALMA 3.1 mm continuum image showing the two detected sources, J1023 and ALMA J102349.1+003824. The white dotted boxes display the field of view shown in the right panels. The ALMA synthesized beam (0.87″ × 0.53″, P.A.=−74.5°) is shown at the bottom right corner. *Right:* Close-up images of J1023 (top) and ALMA J102349.1+003824 (bottom). In both panels, the color scale corresponds to the image with natural weighting with the 3σ contour indicated in white, where σ is listed in Table 2. The black contours are derived from the ALMA image obtained with `robust=0`. Contours range from 3σ to 9σ in steps of 1σ, where σ = 9.1 μJy beam^{-1} for J1023 and σ = 15 μJy beam^{-1} for ALMA J102349.1+003824. The white cross depicts the radio position of J1023 (Deller et al. 2012). A faint emission tail is detected at 3σ level extending south-west of J1023. The synthesized beams for the `robust=0` and natural images are displayed in the bottom left and bottom right corners, respectively (see Table 2). In all panels, the color scale is in units of Jy beam^{-1}.

Table 5. X-ray and millimetre properties of J1023 during the periods of high and low X-ray modes.

X-ray mode	Γ[a]	F_X[b] (10^{-12} erg cm^{-2} s^{-1})	I_ν (μJy beam^{-1})	S_ν (μJy)	Deconvolved Size (″×″)	P.A (°)
High	1.66 ± 0.03	13.8 ± 0.2	74 ± 6	89 ± 13	(0.338±0.202)×(0.250±0.044)	105±8
Low	1.7 ± 0.1	2.1 ± 0.2	117 ± 11	134 ± 23	(0.384±0.245)×(0.260±0.125)	141±45

Notes. [a] Best-fitting photon index for the absorbed power-law model. [b] Unabsorbed flux over the 0.3–10 keV energy band.

3.6. The low-mode ingress and egress timescales

We first examined the low mode ingress and egress times in the *XMM-Newton* observation. For each low-mode episode, we used a simple model for the count rate light curve consisting of four components: a constant level for the high mode (allowing for a different count rate at the entrance and at the exit of the low-mode episode), a linear ingress in the low mode, a constant count rate in the low mode, and a linear egress. This model is similar in some aspects to what is used to model eclipses in binary stars or planetary transits. While we do not expect to accurately describe

each low-mode episode individually, we consider the results in a statistical sense.

We applied this model to each low-mode episode in the *XMM-Newton*/EPIC count rate light curve, which was binned at 10 s, excluding the initial flaring mode of the observation. We performed the same procedure on the *NICER* data from the second night, using again a 10-s time bin. We fit the model to 56 low-mode episodes for *XMM-Newton* and 10 for *NICER*.

As shown in Fig. 8, the ingress time is shorter than the egress time from the low mode ($\sim 80\%$). Interestingly, we observe that the two low-mode instances detected in the NICER data and
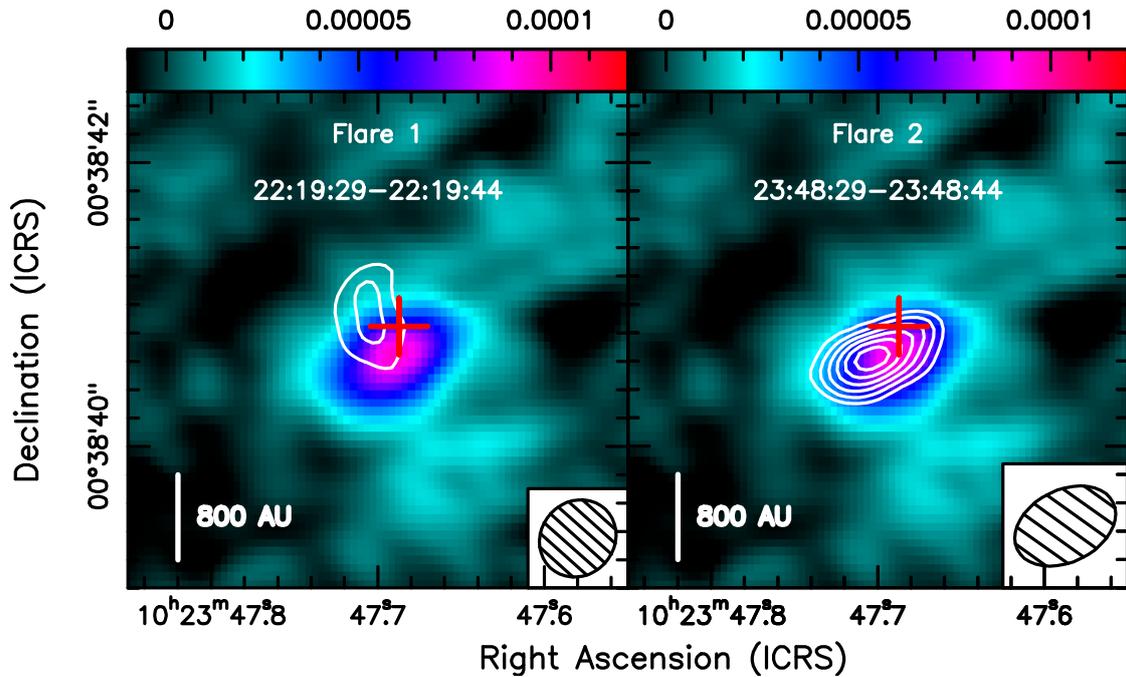
Fig. 7. Contour levels for the millimetre emission detected during 15-s time intervals at the peak of Flare 1 (left panel) and Flare 2 (right panel) are shown using white solid lines overlaid on the naturally weighted ALMA 3.1 mm image extracted using the whole integration time (color scale). These contour levels start at 3σ and increase in steps of 1σ, where σ is the rms of the image, $\sim 90\,\mu$Jy beam^{-1}. Both panels display the same color scale range in units of Jy beam^{-1}. Time intervals (in UTC) are displayed at the top of each panel. The red cross depicts the radio position of J1023 (Deller et al. 2012). The synthesized beams, with extension $0.696'' \times 0.540''$ and position angle P.A.= $-79.92°$ for Flare 1 and $0.931'' \times 0.525''$ and P.A.= $-74.21°$ for Flare 2, are shown at the bottom-right corner of each panel.

Table 6. Millimetre properties of J1023 during the two flaring episodes.

Flare	R.A (ICRS) (hh:mm:ss)	Dec. (ICRS) (°:′:″)	I_ν[a] (μJy beam^{-1})	S_ν[a] (μJy)	Deconvolved Size (″×″)	P.A (°)
Flare 1	10:23:47.705±0.006	00:38:40.92±0.11	426±26	1006±84	(0.96±0.89)×(0.40±0.10)	13.3±6.9
Flare 2	10:23:47.702±0.002	00:38:40.63±0.01	701±62	675±114	. . .[b]	. . .[b]

Notes. [a] These values are measured at the peak of the flares over time intervals of length 15 s and are therefore higher than those obtained in the X-ray mode-resolved analysis and plotted in Fig. 3, where the emission is averaged over longer time intervals. [b] Source marginally resolved in only one direction.

coinciding with short-duration flares detected by ALMA both have comparable ingress and egress times (see the left panel of Fig. 8). This is uncommon and may be related to the detectability of flares at millimetre wavelengths. The distributions of *XMM-Newton* low-mode ingress and egress times are shown in the right panel of Fig. 8. The average logarithmic ingress time is (10.4±6.9) s, which is consistent with the time binning. The average logarithmic egress time is (30.6±8.2) s. We also investigated whether there was any relationship between ingress time, egress time, duration of the low mode, count rate at the beginning and end of the low mode, and count rate in the low mode. However, we did not find any statistically significant correlations.

Although the model we used to describe the low-mode episodes is simple, it is clear that the duration of the ingress time in the low mode is short and consistent with the adopted time binning, and the egress time from the low mode is measurable and longer.

4. Discussion

4.1. The physical picture

Our campaign, along with previous findings, allows us to draw a comprehensive physical picture of the high-low mode switches

in J1023, which involves a permanently-active rotation-powered pulsar, an accretion disc and episodes of discrete mass ejection on top of a compact jet. In the following, we outline the physical scenario while in Sect. 4.2 we will describe in detail the SED modeling in support of our scenario. Fig. 9 shows a visual representation of our scenario. We do not discuss the flaring activity here as it was not covered over a wide energy range.

We assume that during the high mode the accretion flow is kept just beyond the light cylinder radius ($\simeq 80$ km) by the radiation pressure of the particle wind from an active rotation-powered pulsar (Papitto et al. 2019). This causes the innermost region of the truncated, geometrically thin accretion disc to be replaced by a radiatively inefficient, geometrically thick flow, as expected for low-accretion rates (Narayan & Yi 1994). In this configuration, synchrotron radiation at a shock front that forms where the pulsar wind interacts with the inner flow produces the bulk of the X-ray emission as well as X-ray, UV, and optical pulsed emission (Papitto et al. 2019; Veledina et al. 2019). The collision of high-energy charged particles from the pulsar wind with the inflowing matter in the disc increases the ionisation level of the disc. As a result, the inflowing matter is drawn into the pulsar magnetic field and accelerated, producing a compact jet of plasma that streams out along the direction of the pulsar magnetic field lines. According to our SED modelling, the
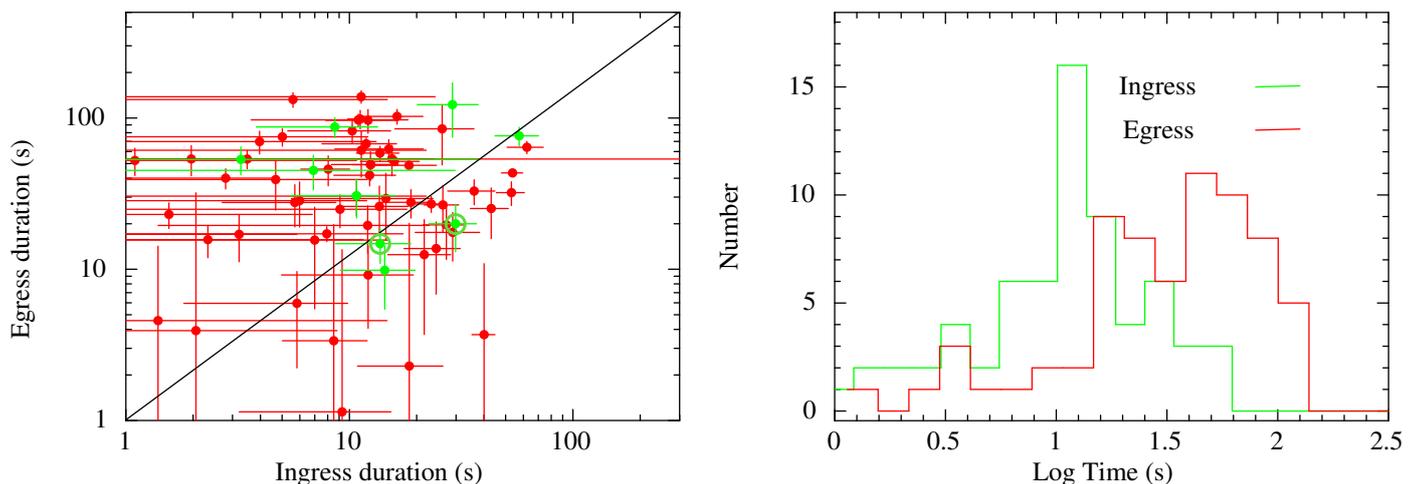
Fig. 8. Results of the statistical analysis of the X-ray mode switching timescales. *Left*: Duration of the low-to-high mode switch (egress) as a function of the duration of the high-to-low mode switch (ingress) computed using data from *XMM-Newton*/EPIC (in red) and *NICER* (green). The circled green points represent the values for the ingress associated with the two millimetre flares detected with ALMA and the subsequent egress. The black solid line indicates where the two quantities are equal. *Right*: distribution of the low-mode ingress (in green) and egress (in red) times in logarithmic scale from *XMM-Newton* and *NICER* data.

corresponding jet synchrotron spectrum is optically thick up to the mid-infrared band and breaks to optically thin above a frequency of $(2.4^{+1.9}_{-1.0}) \times 10^{13}$ Hz, giving only a small contribution at X-ray energies ($\sim$8–18% in the 0.3–10 keV band; see Fig. 11 and Table 8).

The switch from the high to the low mode can be connected to the occurrence of short millimetre flares. There is strong evidence that at least one such flare is directly involved in triggering the switch (see Fig. 3). We interpret these flares as the fingerprint of a discrete mass ejection that marks the removal of the inner flow (see Sect. 4.1.1), similar to what has been observed in other black-hole and NS X-ray binaries (e.g. Cyg X-3, Circinus X-1, V404 Cygni, MAXI J1535-571, MAXI J1820+091; Egron et al. 2021; Fender et al. 1998, 2023; Russell et al. 2019; Homan et al. 2020), albeit in different accretion regimes. As soon as the inner flow is expelled in the discrete ejection, synchrotron emission from the shock no longer takes place, resulting in a drop of the X-ray flux and the quenching of X-ray, UV and optical pulsations. The system enters the low mode.

During the low mode, the pulsar wind can still penetrate the accretion disc, collide with the inflowing matter, and launch the compact jet, contributing to the multiband emission in the same way as in the high mode. The X-ray emission is likely to be (almost) entirely from optically thin synchrotron radiation from this jet (Fig. 11, right panel), with a power-law index of $\alpha = -0.78 \pm 0.04$ (where the flux density F_ν scales with the observing frequency ν as $F_\nu \propto \nu^\alpha$; see Table 8). At the same time, the emission associated with the discrete ejection progressively shifts towards lower frequencies as the ejected material expands adiabatically during the low mode and quickly evolves from optically thick to optically thin (Bogdanov et al. 2018). This emission component has a steep spectrum ($\alpha = -0.8^{+0.3}_{-0.4}$) and provides an additional flux contribution above that of the underlying optically-thick emission from the compact jet at frequencies below the millimetre band (see Figs. 1 and 3).

Eventually, the flow from the disc starts to refill the inner regions just outside the NS light cylinder on a thermal timescale (tens of seconds) due to its advection-dominated nature. The refilling of the disc re-establishes the region of shock with the pul-

sar wind, leading to increased emission and pulsations at X-ray, UV, and optical frequencies (Papitto et al. 2019; Miraval Zanon et al. 2022; Illiano et al. 2023). The system thus makes a switch back to the high mode.

As shown in Sect. 3.6, the low mode ingress and egress times show a statistically significant difference, with the average egress time being longer than the median ingress time. In our picture, the ingress in the low mode is caused by the ejection of the innermost regions of the disc. This will occur on a dynamic timescale. We can estimate the distance at which the innermost edge of the disc in J1023 must recede away from the NS at the high-to-low mode switch by assuming that most of the X-ray emission in the low mode is due to the jet and hence imposing that the luminosity of the synchrotron emission at the shock front is at most, say, 10% of that observed in the low mode. This gives a radial distance of $r_{\text{low}} = [L_{\text{sd}}/(0.1 L_{\text{X,low}})]^{0.5} r_{\text{LC}} \approx 20 \, r_{\text{LC}} \approx 1600$ km ($L_{\text{sd}} = 4.43 \times 10^{34}$ erg s^{-1} is the spin-down luminosity; Archibald et al. 2013). This value should be considered as a lower limit: at larger radii, the X-ray luminosity due to the shock would be even smaller. The dynamic timescale is $\sqrt{r^3/(GM)} \sim 0.1$ s at $20 \, r_{\text{LC}}$. Observations from *XMM-Newton* and *NICER* show that current X-ray instruments are capable of probing mode switching in J1023 on timescales as short as $\sim$10 s. In the future, proposed X-ray missions that offer instruments with much larger collecting areas, high throughput, and excellent time resolution, such as the New Advanced Telescope for HIgh-ENergy Astrophysics (*NewAthena*; Nandra et al. 2013), the enhanced X-ray Timing and Polarimetry mission (*eXTP*; Zhang et al. 2016) and the Spectroscopic Time-Resolving Observatory for Broadband Energy X-rays (*STROBE-X*; Ray et al. 2019), would be able to sample the switch on a time scale <10 s and test our predictions.

The ejection and replenishment of the inner flow in J1023 during mode switches from high to low mode and from low to high mode are reminiscent of the ejection of the X-ray corona into a jet and subsequent replenishment observed in the Galactic microquasar GRS 1915+105 (Méndez et al. 2022). A previous study has demonstrated that, in the case of GRS 1915+105, the outer disc steadily refills the central part of the system on a viscous timescale (Belloni et al. 1997). The rise time is the duration
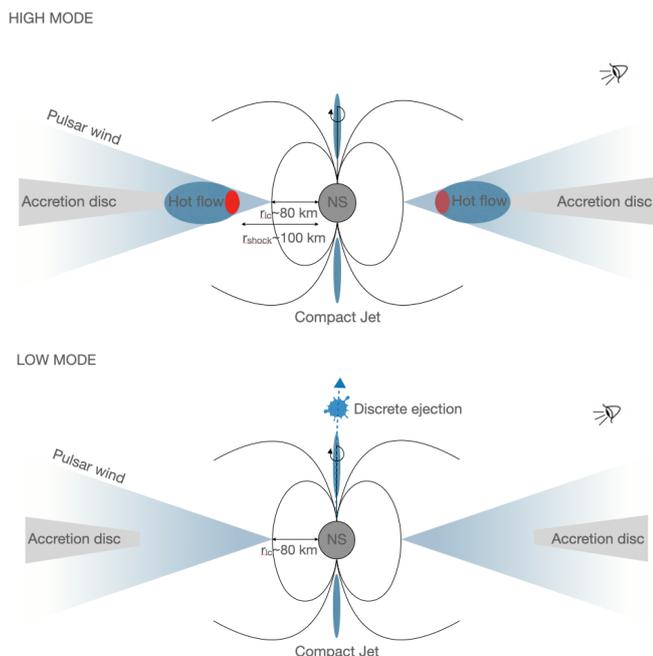
Fig. 9. Schematic visual representation of the evolution of the inner flow into an outflow at the switch from the high to the low X-ray emission mode. When the system is in the high mode (top panel), a small-size inner flow is present, together with a faint steady jet that gives rise to the observed low-level radio and millimetre emission. As the pulsar rotates, the pulsar wind wobbles around the equatorial plane (see e.g. Bogovalov 1999) and shocks off the electrons in the inner flow at two opposite sides (red spots) at a distance that is slightly larger than the light cylinder radius ($\simeq$80 km). At each pulsar rotation, synchrotron emission at the shock at X-ray, UV and optical frequencies is modulated at the spin period at one side (bright red spot), while it is absorbed by material in the inner flow at the other side (light red spot) (Papitto et al. 2019). When the system makes a switch to the low mode (bottom panel), a bright discrete ejection is launched on top of the compact jet, the inner flow disappears and the shock emission is quenched. For displaying purposes, only the inner regions of the compact jet are represented in both panels. The direction of the NS magnetic axis is assumed to be misaligned with respect to the plane of the disc. Instead, the jet is aligned with the spin axis, as represented in the figure.

it takes for the heating front to propagate through the central disc. By assuming a subsonic velocity for the heating front, with the sound speed c_S calculated in the cool ($\lesssim 6 \times 10^6$ K) disc state, we can estimate the rise time to be $r_{\text{low}}/c_S \approx 20$ s for J1023.

In the above picture, we have assumed that the emission from the compact jet remains relatively constant over time, but it is also possible that the jet could be partially disrupted by the discrete ejection of plasma at the switch from high to low mode. However, if the ejection is not energetic enough to overcome the magnetic fields and pressures within the jet, or if it is not dense enough or well-aligned to effectively interact with the jet, then the jet would quickly re-establish itself and appear as if it had never turned off. In either cases, the jet would still contribute the same amount of flux in both modes, especially in the radio band where the emission is produced at greater distances from the NS (on the order of light-minutes to light-hours; Chaty et al. 2011) and therefore any changes are on much longer timescales than the mode switching.

4.1.1. Millimetre flares as the fingerprint of discrete ejecta

Starting from the time scales of the first millimetre flare that occurred during the second night (which has more accurate start and end times than the second flare) and the typical time scales of the radio flares that occurred during the first night, we attempted to reproduce the light curves of similar flares by assuming they are caused by the motion and expansion of a blob of plasma accelerated near the pulsar. Following the work of Fender & Bright (2019), we assumed that a typical discrete ejection expansion is well-described by the van der Laan model (van der Laan 1966)[12]. Since no flare in this study was observed simultaneously at two different frequencies, we are unable to properly constrain the model parameters. However, we are able to check whether we could reproduce flares with peak flux densities and durations that are consistent with what we observed. We assumed that the blob is launched a few hundred kilometres away from the NS with a mildly relativistic velocity ($v \approx 0.05\,c$), and expands linearly over time. We also assumed a magnetic field that scales with the distance from the compact object as $B \propto R^{-1}$, with a magnetic field at the launching site of the order of 10^5 G (see Eq. 6 by Papitto et al. 2019 for an expression of the post-shock magnetic field of an isotropic pulsar wind). Additionally, we considered an electron number density of 10^{11}–10^{12} cm^{-3}, which is consistent with the lower limit estimated from high-resolution X-ray spectroscopy (Coti Zelati et al. 2018). Our calculations show that we can reproduce flares that last for a few seconds and reach a peak flux density of the order of 1 mJy at the ALMA centroid frequency. Furthermore, these flares would result in flares that last for a few tens of seconds and reach a peak flux density of the order of 0.2 mJy at the VLA centroid frequency. These results are consistent with the predictions of the van der Laan model for an expanding blob of plasma.

Although we cannot firmly prove the true origin of the flares, we can ascribe the non-detection of flares in five out of the seven high-to-low-mode switches covered by ALMA to the variation in the intrinsic properties of the ejected material. These include the size, density, temperature, electron energy distribution, and opening angle of the ejected material. In general, smaller, less dense, and cooler ejecta that travel at slower bulk speeds tend to produce fainter millimetre emission (see e.g. Tetarenko et al. 2017; Wood et al. 2021). Additionally, the distribution of the ejected material along the line of sight can also affect the detectability of millimetre flares through absorption and scattering effects (this is likely the main reason for the non-detection of pulsed radio emission as well; see Sect. 4.1.2). Overall, a combination of these factors can explain the varying emission properties observed at millimetre and radio frequencies during (and following) different high-to-low-mode switches. These variations are likely to affect the time it takes for the inner flow to restore itself and produce the shock emission, resulting in the observed differences in duration among the low-mode episodes.

4.1.2. On the non-detection of radio pulsations

The non-detection of radio pulsations could be due to 'intrinsic' phenomena within the pulsar magnetosphere (i.e. irrespective of the presence of external drivers such as accreting material) such as intermittency and/or nulling (see e.g. Weng et al. 2022 for recent similar considerations for the system LS I +61 303). However, these phenomena were not observed during extensive radio

---

[12] The calculations we made are based on van der Laan (1966), and are described in a Jupyter-notebook available at https://github.com/robfender/ThunderBooks/blob/master/Basics.ipynb

timing campaigns when the system was in the radio pulsar state (e.g. Archibald et al. 2013; Stappers et al. 2014), so they are unlikely to be the cause of the non-detection. Alternatively, the non-detection of pulsations may be due to the presence of matter enshrouding the system (see also Coti Zelati et al. 2014; Stappers et al. 2014). In this scenario, we can estimate a lower limit on the mass transfer rate from the companion star by requiring that the optical depth due to free-free absorption is larger than unity throughout the duration of the FAST observation. The analytical expression for the free-free optical depth is given by:

$$\tau_{\mathrm{ff,1.25\,GHz}} \simeq 2.126 \times 10^{22} \times$$

$$\times \frac{\dot{m}_{\mathrm{C}}^2 (M_{\mathrm{NS}} + M_{\mathrm{C}})^2 (X + 0.5Y)^2 (9.157 + 2\ln T_4)}{T_4^{3/2} v_8^2 P_{\mathrm{orb}}^2 (M_{\mathrm{NS}} + 0.538 M_{\mathrm{C}})^3} \ , \qquad (2)$$

where $\dot{m}_{\mathrm{C}}$ is the mass transfer rate in units of $M_\odot\,\mathrm{yr}^{-1}$, M_{NS} and M_{C} are the mass of the NS and the companion star, respectively, X and Y are the mass fraction of hydrogen and helium, respectively, T_4 is the plasma temperature in units of 10^4 K, v_8 is the velocity of the particle wind in units of $10^8\,\mathrm{m\,s}^{-1}$ and P_{orb} is the orbital period in hours (Burgay et al. 2003; Iacolina et al. 2009). We assume $M_{\mathrm{NS}} = 1.65\,M_\odot$, $M_{\mathrm{C}}= 0.24\,M_\odot$, P_{orb}=4.75 h (Archibald et al. 2009), v_8=1, X=0.7 and Y=0.3[13], and v_8=1. In order to have $\tau_{\mathrm{ff,1.25\,GHz}} \simeq 1$, and therefore not detect the radio signal due to free-free scattering, we estimate $\dot{m}_{\mathrm{C}} \gtrsim 10^{-11}\,M_\odot\,\mathrm{yr}^{-1} \approx 6 \times 10^{14}\,\mathrm{g\,s}^{-1}$. This value is a factor of $\gtrsim$10–60 larger than the mass accretion rate estimated based on a systematic analysis of the X-ray aperiodic variability of J1023 in the sub-luminous X-ray state (Linares et al. 2022). This implies that a large fraction of the accreting mass does not reach the compact object's surface and is instead ejected from the system. It is worth mentioning that the predicted mass transfer rate for J1023, based on the transfer of mass through the loss of orbital angular momentum, is $\sim 10^{-11}\,M_\odot\,\mathrm{yr}^{-1}$ (Verbunt 1993).

4.2. Spectral Energy Distributions

4.2.1. Data preparation

We extracted the SEDs separately in the high and low mode and fit them using a model that reflects the physical scenario proposed in Sect. 4.1.

The NIR, optical and UV data obtained during Night 2 were de-reddened assuming $A_V = 0.17\pm0.01$ mag, calculated from the *XMM-Newton* estimate of N_{H} using the N_{H}/A_V relation reported by Foight et al. (2016). The absorption coefficients in the other bands were estimated using the equations reported by Cardelli et al. (1989), and are listed in the last column of Table 7.

For the low-mode SED, we considered optical data acquired between MJD 59392.01085 and 59392.01434, totaling three consecutive 60-s integration images in each band; the *J*-band flux is the average of the fluxes measured with NTT/SOFI while the source was in the low mode, according to our *XMM-Newton* monitoring; the UV (uvm2) flux was measured on MJD 59392.01302; radio flux densities are taken from the VLA observation on 2021 June 3–4; the millimetre flux density was derived from stacking all the ALMA images acquired during the

---

[13] We note that our assumption on X and Y should be regarded as a zeroth-order approximation since a recent study by Shahbaz et al. (2022) has shown that the chemical abundances of the companion star of J1023 are different from those found in most X-ray binaries. However, since $\dot{m}_{\mathrm{C}} \propto (X + 0.5Y)^{-1}$, the lower limit on $\dot{m}_{\mathrm{C}}$ only increases by a factor of a few if smaller values of X and Y are assumed.

Table 7. Central frequencies (ν_c), flux densities corrected for interstellar absorption and the adopted absorption coefficients (A_ν) used for the SEDs.

Band	ν_c (Hz)	Flux Density (mJy)		A_ν (mag)
		Low mode	High mode	
Radio	1.00×10^{10}	0.158 ± 0.009	0.064 ± 0.006	–
mm	9.75×10^{10}	0.133 ± 0.023	0.089 ± 0.013	–
K	1.40×10^{14}	–	1.17 ± 0.32	0.02 ± 0.03
J	2.39×10^{14}	1.14 ± 0.13	1.12 ± 0.16	0.05 ± 0.03
z	3.28×10^{14}	1.35 ± 0.28	1.34 ± 0.27	0.08 ± 0.01
i	3.93×10^{14}	1.32 ± 0.23	1.20 ± 0.21	0.11 ± 0.01
r	4.81×10^{14}	1.09 ± 0.11	1.03 ± 0.11	0.14 ± 0.01
g	6.29×10^{14}	0.87 ± 0.10	0.84 ± 0.10	0.20 ± 0.01
$uvm2$	1.34×10^{15}	0.10 ± 0.01	0.18 ± 0.02	0.52 ± 0.01

low modes. No *K*-band observations have been acquired during the low mode. The unabsorbed X-ray flux was calculated as the average flux during all periods of low mode.

For the high-mode SED, we considered *K*-band data acquired between MJD 59392.00237 and 59392.00289, and then from MJD 59392.00593 to 59392.00832 (i.e. all the images in which J1023 is detected, 15×15 s); the *J*-band flux is the average of all the fluxes measured with NTT/SOFI while the source was in the high mode, according to our XMM-Newton monitoring; for the optical *griz* bands, we considered one 60-s image for each band, at MJD 59392.00528; the UV (uvm2) flux was acquired on MJD 59392.00413; radio flux densities are taken from the VLA observation on 2021 June 3–4; the millimetre flux density was derived after stacking all the ALMA images acquired during the high mode episodes. The unabsorbed X-ray flux was calculated as the average flux during all periods of high mode.

4.2.2. Model setup

• *Low mode.* To perform the fit to the SED, we used a model comprising a blackbody of an irradiated star and a multi-colour accretion disc, together with a broken power law to describe the optically thick and thin components of the synchrotron emission from the compact jet. In addition, we considered a power law to model the optically thin emission from the discrete ejecta at all frequencies. For the stellar component, we have considered an irradiated star model (see Eqs. 8 and 9 of Chakrabarty 1998) where the surface temperature of the star (T_*) is allowed to vary and the distance to J1023 (D), the radius of the companion star (R_c), the binary separation (a), the irradiation luminosity (L_{irr}) and the albedo of the star (η_*) are fixed to known (or reasonable) values: $D = 1368$ pc (Deller et al. 2012), $R_c = 0.43\,R_\odot$ (Archibald et al. 2009), $\eta_* = 0.1$, and $a = [G(M_{\mathrm{NS}} + M_{\mathrm{C}})P_{\mathrm{orb}}^2/(4\pi)^2]^{1/3}$, where $M_{\mathrm{NS}} = 1.65 M_\odot$ is the NS mass, $M_{\mathrm{C}} = 0.24 M_\odot$ is the mass of the companion star, $P_{\mathrm{orb}} = 4.75$ hrs is the binary orbital period and G is the gravitational constant. L_{irr} was fixed to 6.5×10^{33} erg s^{-1}, the value estimated by Shahbaz et al. (2019) from the difference of the temperatures of the illuminated and dark sides of the companion star of J1023. This value corresponds to 14% of the pulsar spin-down luminosity (Archibald et al. 2013), and is of the same order of magnitude as the X-ray and gamma-ray luminosities in the sub-luminous X-ray state. For the multi-color accretion disc model (Eqs. 10–15 by Chakrabarty 1998), we allowed the inner radius of the accretion disc where the optical/UV emission becomes relevant ($r_{\mathrm{in,opt/UV}}$) to vary, while we fixed the X-ray albedo of the disc to 0.95 (Chakrabarty 1998) and the mass transfer rate to $10^{-11}\,M_\odot\,\mathrm{yr}^{-1}$. This is the value predicted for an X-ray binary system with a short orbital period hosting a main-

sequence star and transferring mass through loss of angular momentum (Verbunt 1993), and is consistent with the lower limit estimated from the non-detection of radio pulsations (Sect. 2.6). The broken power-law component has the normalisation F_0, the two slopes α_1 and α_2 and the break frequency ν_{break} as free parameters; the power law associated with the emission from the discrete ejecta has the normalisation $F_{\text{thin},10}$ (calculated at a frequency of 10 GHz) and the slope α_{thin} as free parameters.

• *High mode.* We used a more complicated model following the physical picture explained above. In particular, we considered that the X-rays are produced by the sum of the optically thin component of the synchrotron emission from the base of the compact jet and the synchrotron emission from the region of shock between the pulsar wind and the inner flow. For the latter, we used the analytical expression for the synchrotron spectrum by Chevalier (1998) (see his Eq. 1). For the emission at lower frequencies, we included the blackbody of the irradiated star (fixing L_{irr} to 6.5×10^{33} erg s^{-1}), the multi-colour blackbody of the accretion disc, and the optically thick component of the synchrotron emission from the compact jet. The parameters of the fit are T_*, ν_{break}, α_1, α_2, F_0, $r_{\text{in,opt/UV}}$, ν_{sync}, α_{sync} and F_{sync}, where ν_{sync}, α_{sync}, F_{sync} are the peak frequency of the synchrotron emission, the slope of the optically thin synchrotron emission and the normalisation of the synchrotron emission, respectively.

Employing both data sets (high and low mode), we performed an MCMC sampling of the posterior probability density function for the parameter space of the two models simultaneously (since some of the free parameters are shared by both models). We used a Gaussian prior for the temperature of the star centered on the value measured by Shahbaz et al. (2022) during the disc state, $T_* = (6128 \pm 33)$ K. Gaussian priors have also been used for the parameters α_1 (centered on 0.2 ± 0.2) and α_2 (centered on -0.7 ± 0.2), following the results of Bogdanov et al. (2018). We note that we also tried wider Gaussian priors for these parameters, resulting in wider posterior distributions with medians compatible with the results below within 1–2σ. For all other parameters, we used uniform priors in very wide intervals to sample a large region of the parameter space (see last column of Table 8). This is of great importance to minimise the probability that the actual source parameters fall outside the region sampled by the chosen priors.

4.2.3. Results

The results of the fit are reported in Table 8 and are summarized in the following paragraphs. All the parameters have been estimated as the median of the marginal posterior distributions, with 1σ credible intervals coming from the 16–84th percentiles of the posterior distributions (see Fig. 10 for the histograms of the parameter samples). Most of the marginal posterior distributions of the parameters shown in Fig. 10 are nearly Gaussian, meaning that they are almost symmetrical. Fig. 10 also shows a strong correlation between ν_{sync} and F_{sync}, and between F_0 and α_1. This is however not surprising considering the scarce number of points at the lowest frequencies and the impossibility to constrain quantities such as ν_{break} and ν_{sync}, due to numerous overlapping components at infrared and optical frequencies. In particular, we note that F_{sync}, ν_{sync} and α_{thin} have a non-symmetrical posterior distributions, with long tails towards the upper or the lower limit of the chosen interval for the prior, depending on the parameter. However, the peak of their distributions is well determined (see Fig. 10). To estimate the goodness of the fit, we

used the Bayesian p-value (reported in the last line of Table 8; Lucy 2016). The p-value is 0.78 for the high mode and 0.07 for the low mode, meaning that the results of the fit are indeed acceptable (with a slight indication of overestimated and underestimated uncertainties for the high and low mode fit, respectively).

The synchrotron emission caused by the shock has a higher flux density in the optical band than the average pulsed flux density fraction of ∼1% estimated by Papitto et al. (2019), which makes our scenario plausible. In particular, we find that the shock contributes ∼3% of the emission in the optical band in the high mode, which is similar to the contribution of the optically thin component of the compact jet emission. In the *XMM-Newton*/EPIC 0.3–10 keV range, the shock accounts for ∼83% of the emission, while the jet only contributes ∼17% of the flux in the high mode.

4.3. Considerations on optical polarisation measurements and predictions of X-ray polarisation

The average optical polarisation reported in this work is similar to levels previously measured for this source (Baglio et al. 2016; Hakala & Kajava 2018). Since the polarisation level is <1%, it could have multiple origins. Given the lack of modulation of the Stokes parameters with the orbital period, it is unlikely that the source of the polarisation is scattering of radiation in any region of the system (such as the surface of the accretion disc), in contrast to previous suggestions (Baglio et al. 2016). We identify two possible main emission mechanisms for the polarised emission, both of which are non-thermal: optically thin synchrotron emission from the compact jet, or synchrotron emission at the shock between the pulsar wind and the accretion inflow, which also gives rise to the observed optical pulsations (as also suggested by Hakala & Kajava 2018). The jet flux density in the r-band is ∼0.02 mJy, corresponding to a fractional contribution to the total flux in the same band of ∼2.4% and ∼2% in the high and low modes, respectively. In the high mode, where the polarisation level measured in the R-band is 0.65 ± 0.43%, this translates into a polarisation level of the jet emission of ∼26% (or ∼37% if the average polarisation level of 0.92% is considered instead). In the low mode, the jet emission is instead intrinsically polarised at a level of ∼17%. Following Shahbaz (2019) and references therein, we estimate a level of ordering of the magnetic field lines of ∼30% (considering the case of an optically thin synchrotron emission with a spectral slope of ∼−0.78, as obtained from our fit and averaging across modes; see Table 8). This indeed indicates a highly ordered magnetic field and suggests that tMSPs might have a more ordered magnetic field at the base of the jet than other NS and BH X-ray binaries (XRBs) (Russell & Fender 2008; Baglio et al. 2014; Russell et al. 2016; Baglio et al. 2020). Based on our picture, this could be ascribed to the presence of a continuous, steady flow of plasma near the pulsar, which may help to maintain a more ordered magnetic field structure at the base of the jet.

Assuming that the observed optical polarisation is due to this emission component and that the same population of accelerated electrons in the jet produces optically thin synchrotron radiation at all frequencies above the break frequency, we can predict a polarisation level in the X-ray band (in the 2–8 keV energy range of the Imaging X-ray Polarimetry Explorer, *IXPE*; Weisskopf et al. 2016; Soffitta et al. 2021) due to the jet of ≈17% in the low mode, where the jet contributes to ∼100% of the flux according to our SED modeling.

Alternatively, the observed optical polarisation might originate from synchrotron radiation at the region of shock between

Table 8. Results of the model fit of the SED in low and high modes. The median values of the posterior distributions of the model parameters are reported, along with lower and upper uncertainties. These uncertainties correspond to the 15.9th and 84.1th percentiles of the posterior distributions for each parameter. The last column reports the prior bounds that were used for all parameters; $\mathcal{N}(\mu, \sigma)$ is a normal distribution centered in μ and with variance σ^2, and $\mathcal{U}(a, b)$ is a uniform distribution in the (a, b) interval.

Component	Parameter	Posterior		Prior bounds
		Low mode	High mode	
Irradiated star	T_* (K)	$6141.05^{+32.91}_{-30.37}$		$T_* \sim \mathcal{N}(6128, 33)^*$
Accretion disc	Log $[r_{\mathrm{in,opt/UV}}$ / 1 cm]	9.49 ± 0.02		Log $r_{\mathrm{in,opt/UV}} \sim \mathcal{U}(7, 12)$
Compact jet	Log $[\nu_{\mathrm{break}}$ / 1 Hz]	13.40 ± 0.26		Log $\nu_{\mathrm{break}} \sim \mathcal{U}(10, 14)$
	α_1	0.18 ± 0.06		$\alpha_1 \sim \mathcal{N}(0.2, 0.2)^\dagger$
	α_2	-0.78 ± 0.04		$\alpha_2 \sim \mathcal{N}(-0.7, 0.2)^\dagger$
	Log $[F_0$ / 1 mJy]	$-0.59^{+0.15}_{-0.17}$		Log $F_0 \sim \mathcal{U}(-2, 0)$
Shock emission	Log $[\nu_{\mathrm{sync}}$ / 1 Hz]	–	$14.34^{+0.44}_{-0.30}$	Log $\nu_{\mathrm{sync}} \sim \mathcal{U}(12, 16)$
	α_{sync}	–	-0.61 ± 0.01	$\alpha_{\mathrm{sync}} \sim \mathcal{U}(-0.9, -0.4)$
	Log $[F_{\mathrm{sync}}$ / 1 mJy]	–	$-1.11^{+0.18}_{-0.27}$	Log $F_{\mathrm{sync}} \sim \mathcal{U}(-3, 2)$
Discrete ejecta	α_{thin}	$-0.78^{+0.24}_{-0.43}$	–	$\alpha_{\mathrm{thin}} \sim \mathcal{U}(-1.5, 0)$
	Log $[F_{\mathrm{thin},10}$ / 1 mJy]	-1.03 ± 0.05	–	Log $F_{\mathrm{thin},10} \sim \mathcal{U}(-5, 2)$
	Bayesian p-value	0.07	0.78	–

Notes. * Value from Shahbaz et al. (2022). $\dagger$ Value from Bogdanov et al. (2018).

the pulsar wind and the accretion flow. In this scenario, polarisation should only be detected during the high mode. Unfortunately, the significance of our polarisation results obtained in the high and low modes separately is not high enough to verify this, as the results are compatible with each other within 1σ ($0.36^{+0.27}_{-0.35}\%$ in the low mode and $0.65 \pm 0.43\%$ in the high mode). The fractional flux contribution of the shock in the r-band according to the SED modeling in the high mode is $\sim 4.8\%$, which translates into a linear polarisation of the emission of the shock of ~ 15–20%, with peaks of up to 65–90% at the pulsations (in fact, the fraction of pulsed radiation is typically of $\sim 1\%$; Papitto et al. 2019). This prediction could be tested using next-generation optical high-time resolution polarimetric instruments (Ghedina et al. 2022). In the X-rays instead, we predict a fractional flux contribution of the shock emission of $\sim 90\%$ in the *IXPE* energy range, which converts into an intrinsic linear polarisation level of ≈ 12–17%. This could be detected in an *IXPE* observation of ~ 460 ks (assuming J1023 spends 70% of the time in the high mode).

In both scenarios, the validity of these predictions depends on the assumption that the optical polarisation is solely caused by synchrotron radiation from the jet or shock. However, if the observed polarisation is due to a combination of these factors or if other processes are at play that are not being considered (such as scattering on the disc surface contributing to the modulation with a low SNR in our measurements), these predictions may need to be revised.

4.4. The millimetre continuum emission of J1023 and other X-ray binary systems

We have reported the detection of millimetre continuum emission for the first time from J1023 (and from a tMSP in general) using ALMA observations at ≈ 100 GHz. The millimetre emission is unresolved, implying a size for the emission region smaller than $\approx 6 \times 10^{15}$ cm (this corresponds to $\approx 7 \times 10^4$

times the orbital separation of the system; Archibald et al. 2013). Millimetre/sub-millimetre continuum emission has been firmly detected from a number of transiently accreting stellar-mass black holes (Paredes et al. 2000; Ogley et al. 2000; Fender et al. 2000, 2001; Ueda et al. 2002; Russell et al. 2013b; van der Horst et al. 2013; Tetarenko et al. 2015, 2017, 2019; Russell et al. 2020; de Haas et al. 2021; Koljonen & Hovatta 2021; Tetarenko et al. 2021; Díaz Trigo et al. 2021) and in three accreting NSs so far: the persistent systems 4U 1728−34 and 4U 1820−30 (Díaz Trigo et al. 2017) and the transient accreting MSP Aql X-1 (Díaz Trigo et al. 2018). In these cases, however, such emission has been detected during accretion states that are seemingly different from the X-ray sub-luminous disc state attained by J1023 at the epoch of our ALMA observations, as detailed below.

In black-hole systems, millimetre continuum emission is typically detected during the rising phase of an X-ray outburst or along the outburst decay, during the "hard" X-ray spectral state. In this state, the X-ray emission is typically dominated by a power-law component that is believed to arise from Compton up-scattering of soft disc photons by a population of hot thermal electrons located either in the innermost region of the accretion flow, or in an extended cloud above the disc (for a recent review, see Motta et al. 2021). At low frequencies, a flat to slightly inverted optically thick spectrum ($\alpha > 0$) has been observed from radio through sub-millimetre frequencies and above and has been associated with partially self-absorbed synchrotron radiation from electron populations in different regions along a compact jet. This spectrum becomes optically thin ($\alpha < 0$) typically around infrared frequencies, resulting in a spectral break (Russell et al. 2013a,c). On the other hand, at very high mass accretion rates (typically close to the outburst peak), these systems can be in a "soft" X-ray spectral state where the X-ray emission is dominated by a thermal component produced in the hot inner regions of the accretion disc (see Motta et al. 2021 and references therein). In the state that immediately precedes or follows the soft state during the outburst (the so-called 'soft-intermediate state'), the optically-thick jet emis-
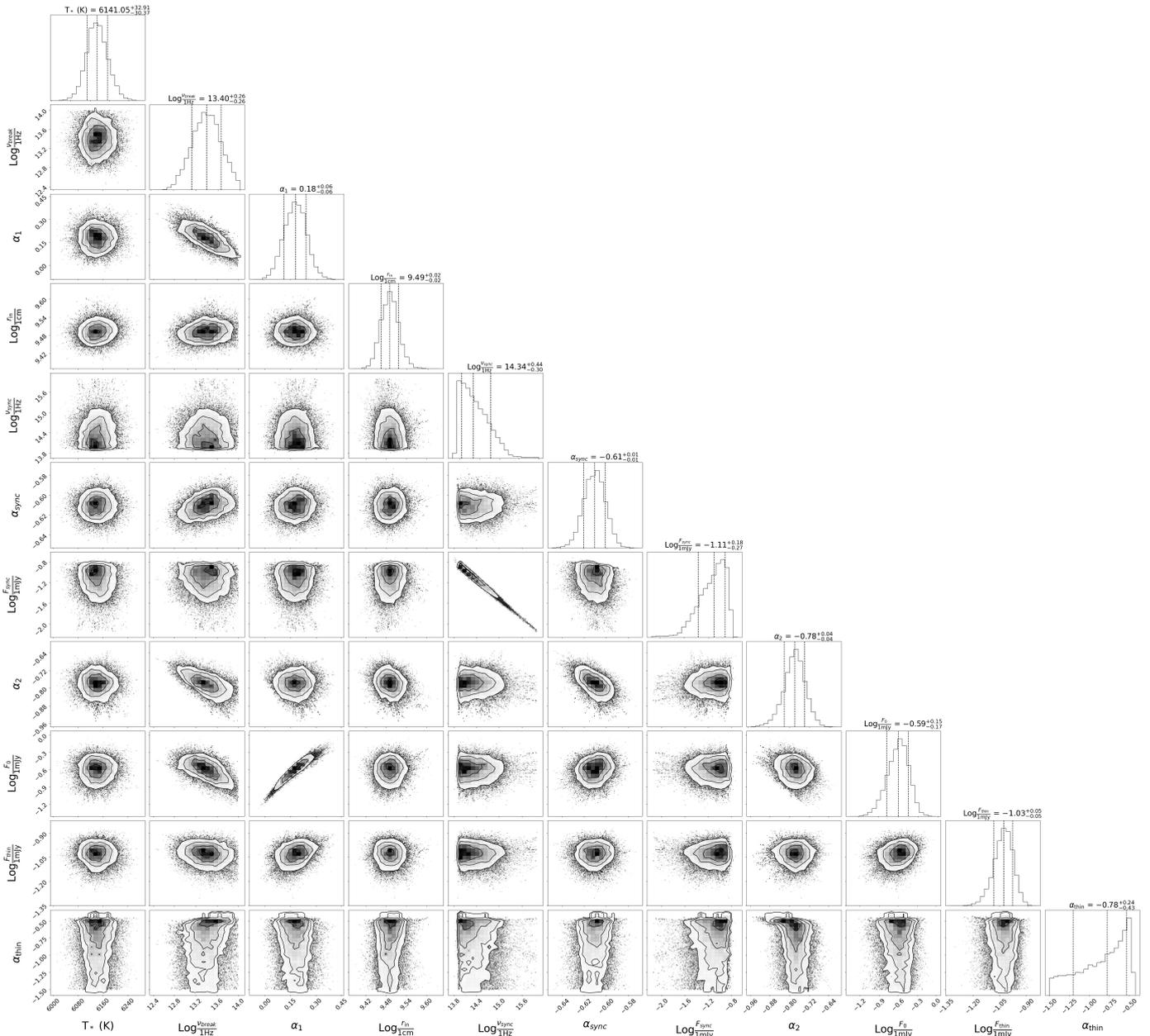
Fig. 10. Corner plot showing the posterior probability distributions of the parameters obtained from the MCMC sampling algorithm. The solid lines in the panels along the diagonal represent the probability density of each parameter. The vertical dashed lines indicate the 16th, 50th, and 84th percentiles of the distributions. The median of the parameter posterior and the 1σ error bars are displayed above each panel. The off-diagonal panels show the two-dimensional posterior distributions with contour lines indicating the 1-, 2-, and 3-σ equivalent bounds.

sion is observed to be quenched altogether, while discrete jet ejecta characterized by an optically thin steep spectrum ($\alpha < 0$) in the radio band can be launched (Fender et al. 2004; Russell et al. 2020) and be accompanied by strong radio variability and bright multi-frequency flaring activity (even in the submillimetre band; Tetarenko et al. 2019).

The picture for NS systems is more diverse (see van den Eijnden et al. 2021 for a recent overview). All three of the above-mentioned NS systems were observed in the millimetre band with ALMA, along with observations at other frequencies, in regimes of high mass accretion rates ($L_X > 5 \times 10^{36}$ erg s^{-1}). 4U 1728−34 was observed during a transition from a hard to a soft state. The low-frequency spectrum was compatible with synchrotron emission from a compact jet and also revealed the

presence of a break from optically thick to optically thin synchrotron radiation at frequencies in the range $10^{13} - 10^{14}$ Hz. In the case of 4U 1820−30, enhanced millimetre emission was detected during a soft X-ray state (the first time millimetre emission has been observed for an accreting NS in the soft state). The spectrum from the radio to the sub-millimetre bands was slightly inverted and showed no evidence for the presence of a spectral break (Díaz Trigo et al. 2017). This indicates emission from a compact jet and supports earlier findings that jets in NS systems do not all appear to be completely suppressed in soft accretion states (Migliari et al. 2004). Aql X-1 was observed five times using ALMA over a time span of ~1.5 months during the decay phase of an X-ray outburst in 2016, covering multiple transitions between distinct accretion states. The spectrum from the
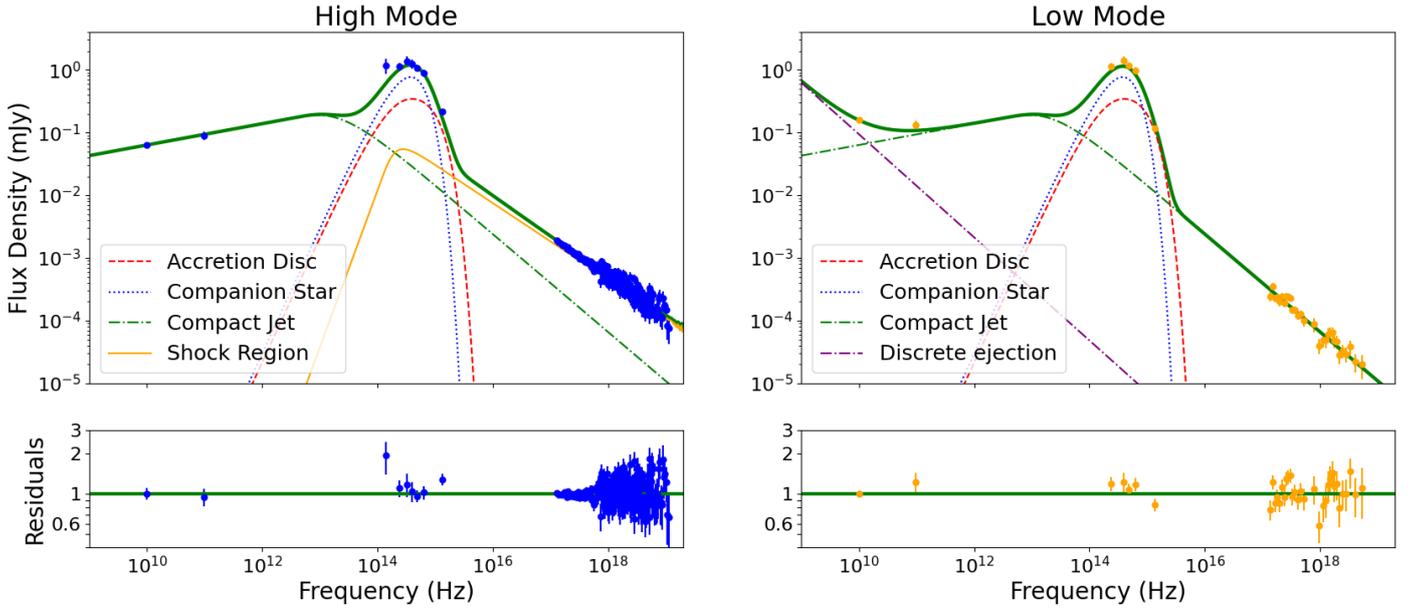
Fig. 11. Broadband (radio to X-rays) SEDs of J1023 during the high and low modes, along with the best-fitting models. Both SEDs were corrected for extinction effects. The red-dashed, blue-dotted, purple-dashed-dotted and orange solid lines represent the contributions of the accretion disc, companion star, discrete ejection and shock region, respectively. The green dashed line represents the compact jet, whose contribution does not vary between the two modes. The green solid line is the sum of all contributions in both SEDs. The ratio between the data points and the best-fitting model is shown at the bottom of each panel.

Table 9. Millimetre and X-ray luminosities of accreting compact objects in X-ray binaries. Values are reported for those systems that have been clearly detected in the millimetre/sub-millimetre bands, have a known distance, and have simultaneous or nearly simultaneous millimetre/sub-millimetre and X-ray observations. Systems above the horizontal line are black-hole systems, while those below the line are NS systems.

Source	Distance (kpc)	Millimetre luminosity[a] (erg/s)	X-ray luminosity[b] (erg/s)	Reference
MAXI J1659−152	6	$(7\pm1)\times10^{31}$	$(1.389\pm0.001)\times10^{37}$	van der Horst et al. (2013)
MAXI J1659−152	6	$(5\pm1)\times10^{31}$	$(4.60\pm0.01)\times10^{37}$	van der Horst et al. (2013)
MAXI J1659−152	6	$<2.6\times10^{31}$	$(4.81\pm0.01)\times10^{37}$	van der Horst et al. (2013)
MAXI J1659−152	6	$<2.7\times10^{31}$	$(4.67\pm0.02)\times10^{37}$	van der Horst et al. (2013)
V404 Cygni	2.39	$(3.64\pm0.06)\times10^{30}$	$(8\pm2)\times10^{34}$	Tetarenko et al. (2019)
V404 Cygni	2.39	$(9.4\pm0.6)\times10^{29}$	$(1.5\pm0.1)\times10^{34}$	Tetarenko et al. (2019)
MAXI J1535−571	4.1	$(4.7\pm0.2)\times10^{32}$	$(2.00\pm0.01)\times10^{38}$	Russell et al. (2020)
MAXI J1535−571	4.1	$(1.0\pm0.2)\times10^{32}$	$(8.6\pm0.1)\times10^{38}$	Russell et al. (2020)
GX 339−4	8	$(1.53\pm0.08)\times10^{31}$	$(1.35\pm0.08)\times10^{36}$	de Haas et al. (2021)
MAXI J1820+070	2.96	$(9.651\pm0.004)\times10^{31}$	$(3.50\pm0.01)\times10^{37}$	Tetarenko et al. (2021)
GRS 1915+105	8.6	2.2×10^{31}	$(2.07\pm0.03)\times10^{37}$	Koljonen & Hovatta (2021)
GRS 1915+105	8.6	2.6×10^{31}	$(2.69\pm0.01)\times10^{37}$	Koljonen & Hovatta (2021)
XTE J1118+480	1.7	6.9×10^{30}	2.4×10^{35}	Fender et al. (2001)
4U 1820−30[c]	6.4	$(1.67\pm0.09)\times10^{30}$	$(3.22\pm0.03)\times10^{37}$	Díaz Trigo et al. (2017)
Aql X-1	5.2	$(2.06\pm0.08)\times10^{30}$	$(1.73\pm0.01)\times10^{37}$	Díaz Trigo et al. (2018)
Aql X-1	5.2	$(1.31\pm0.08)\times10^{30}$	$(9.2\pm0.1)\times10^{37}$	Díaz Trigo et al. (2018)
Aql X-1	5.2	$(2.44\pm0.09)\times10^{30}$	$(6.65\pm0.07)\times10^{36}$	Díaz Trigo et al. (2018)
PSR J1023+0038 (mean)	1.37	$(3.2\pm0.2)\times10^{28}$	$(1.7\pm0.2)\times10^{33}$	This work
PSR J1023+0038 (high)	1.37	$(2.0\pm0.3)\times10^{28}$	$(2.40\pm0.04)\times10^{33}$	This work
PSR J1023+0038 (low)	1.37	$(3.0\pm0.5)\times10^{28}$	$(3.6\pm0.4)\times10^{32}$	This work

Notes. [a] Millimetre luminosities are evaluated at a frequency of 100 GHz. A flat spectrum was assumed to estimate the luminosity for those cases where the flux density is available at other frequencies in the literature, except for MAXI J1820+070 (α=0.25) and 4U 1820−30 (α=0.13).
[b] X-ray luminosities are evaluated over the 1–10 keV energy range and are derived from *Swift*/XRT observations except for the case of J1023, for which values are taken from Table 5. Spectra were extracted using the *Swift*/XRT data products generator (Evans et al. 2009) and fitted using an absorbed power-law model. For the second pair of simultaneous observations of GRS 1915+105, the X-ray luminosity is evaluated using *NICER* obs ID 2596010301.
[c] The millimetre and X-ray observations were separated by 4 days.
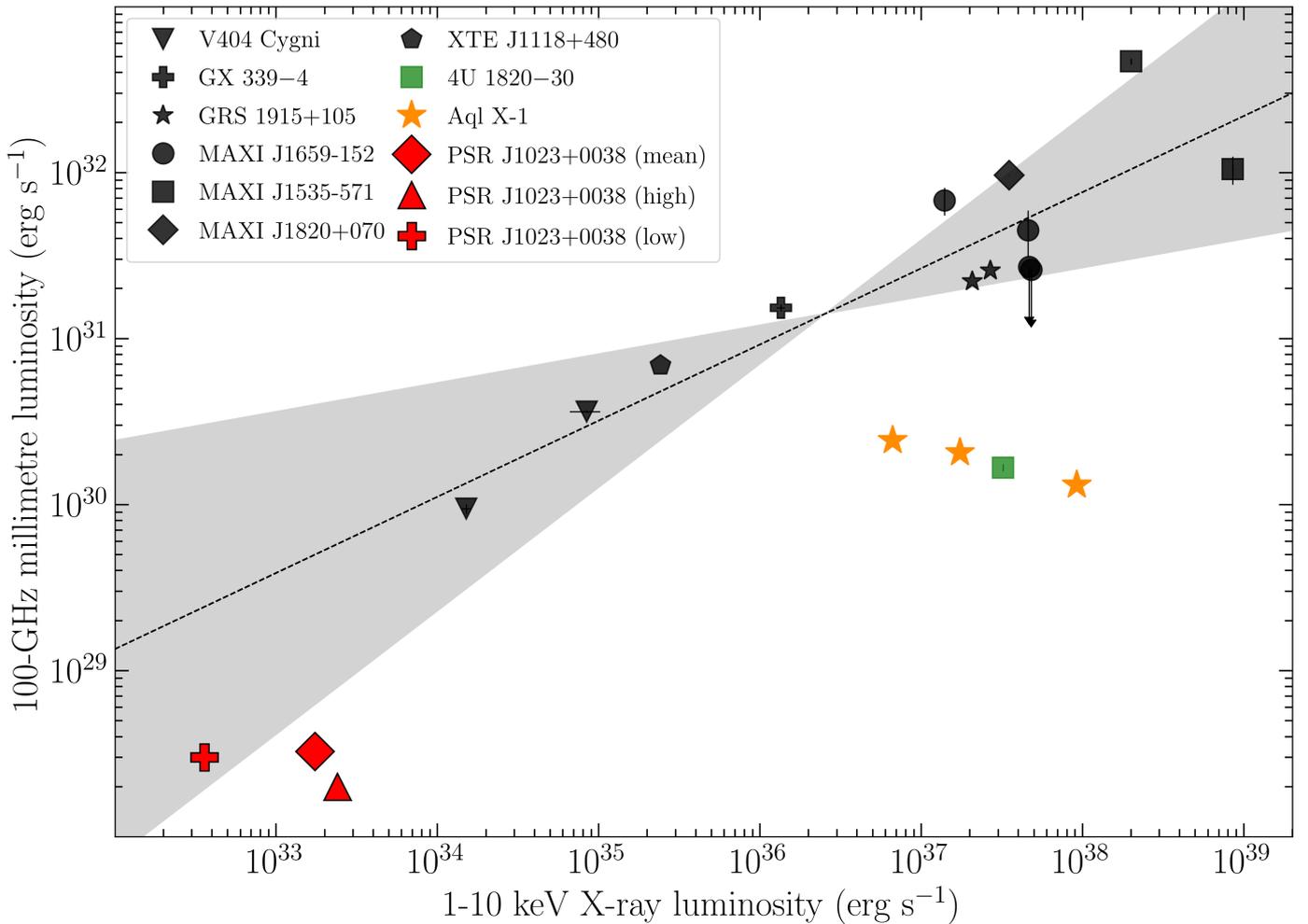
Fig. 12. Millimetre and X-ray luminosities for accreting compact objects in X-ray binaries. BH systems are marked in black. The adopted values for the luminosities are listed in Table 9. The black dashed line and the gray shaded area show the best-fitting slope for the BH correlation and the region on the plane at less than 3σ from the best-fitting slope, respectively (see text for details).

radio to the millimetre bands was again compatible with emission from a compact jet and, for the first time in an accreting NS in a low-mass X-ray binary, a break in the SED was detected at a frequency that varies dramatically depending on the accretion state. Specifically, the break frequency initially decreased from ~100 GHz to less than ~5 GHz during a transition from a hard to a soft state, and then increased again up to a frequency within the range ~30–100 GHz during a transition to a hard state at later stages of the outburst decay (Díaz Trigo et al. 2018).

Unlike all the cases mentioned above, the ALMA observations of J1023 were performed at an epoch when the system did not display any changes in its spectral state and was lingering in a sub-luminous X-ray state ($\approx 10^{33}$ erg s^{-1}). It is worth noting that both the average and the mode-resolved X-ray spectra of J1023 have always been hard and have not shown any substantial changes over the past ten years or so during the sub-luminous X-ray state.

We can compare the millimetre and X-ray luminosities of J1023 with those measured for black-hole and NS systems using quasi-simultaneous millimetre and X-ray observations. These luminosities are reported in Table 9 and plotted in Fig. 12. Despite the relatively small number of existing millimetre/sub-millimetre data for X-ray binaries, Fig. 12 shows that millime-

tre continuum emission has been detected in systems that attain a wide range of X-ray luminosities ($\sim 10^{33}$–10^{39} erg s^{-1}) and that J1023 currently holds the record as the faintest X-ray binary firmly detected in the millimetre band.

The mechanism responsible for the X-ray emission in the two modes in J1023 is clearly different from that at work in black-hole systems in the hard state, so a proper comparison cannot be made. With this in mind, we assessed how the position of J1023 on the $L_{mm} - L_{x}$ plane compares with those of black-hole systems by parameterizing the dependence of L_{mm} upon L_{x} as a relation of the form $\mathrm{Log}L_{mm} - \mathrm{Log}L_{mm,ave} = \alpha + \beta(\mathrm{Log}L_{X} - \mathrm{Log}L_{X,ave})$[14]. We then investigated the shape of the $L_{mm} - L_{x}$ correlation for black-hole systems by performing a Bayesian-based MCMC sampling of the black-hole data (including upper limits) using the linear regression algorithm LIN-MIX_ERR (Kelly 2007). There are three free parameters: the intercept α, the slope β and σ_0, a parameter that accounts for an intrinsic random (Gaussian) scatter of the values around the best-fit model. We calculated the median values of the fit parameters from 10^4 draws from the posterior distribution, and determined the 1σ credible intervals of these parameters using the

---

[14] $L_{mm,ave} = 10^{31.93}$ erg s^{-1} and $L_{X,ave} = 10^{38.03}$ erg s^{-1} are the average values for the detections in our BH sample.

16–84th percentiles of the posterior distributions. We derived $\alpha = -0.04 \pm 0.15$, $\beta = 0.46 \pm 0.09$ and $\sigma_0 = 0.18 \pm 0.13$. The best-fitting slope is consistent with that derived for the $L_{radio} - L_x$ correlation for black-hole systems (Gallo et al. 2018) within the uncertainties. Fig. 12 shows the best-fitting slope (black dashed line) and the region on the plane where the values of L_{mm} and L_X are located at a distance of less than 3σ from the best-fitting slope (gray shaded area). This figure shows that, during the low mode, J1023 follows the same correlation as black-hole systems in the hard state (Bogdanov et al. 2018).

5. Summary and Conclusions

We have presented the results of the largest multi-wavelength campaign ever conducted on the tMSP PSR J1023+0038. This campaign took place in June 2021, while the system was in an active low-luminosity X-ray disc state. Our key findings can be summarized as follows:

• During the first night of observations, flaring activity was detected at X-ray and optical wavelengths, followed by mode-switching behavior in X-rays. The UV emission was significantly fainter in low mode, while the radio continuum emission was brighter. No evidence of pulsed radio emission was detected in either mode. Our observations provide the most stringent limits on the pulsed radio flux density to date.

• During the second night observations, a low-significance variation in the optical polarised signal was detected during mode changes, with a slightly higher polarisation level in the high mode compared to the low mode. The millimetre emission did not strictly follow the X-ray low modes, except for two brief flares. One of these flares occurred at the high-to-low mode switch, while the exact onset time of the other flare could not be determined due to a lack of observational coverage.

• These results allow us to draw a physical picture of high-low mode switches in J1023, involving a rotation-powered pulsar, an accretion disc, and discrete mass ejections on top of a relativistic compact jet. During the high mode, synchrotron radiation at the shock front between the pulsar wind and the inner accretion flow produces most X-ray emission, as well as X-ray, UV, and optical pulsations. The switch to low mode is triggered by discrete mass ejections, resulting in a drop of the X-ray flux and quenching of pulsations. During the low mode, the pulsar wind still penetrates the accretion disc and launches a compact jet, contributing to the multiband emission in the same way as in the high mode. Eventually, the flow from the disc refills the inner regions outside NS light cylinder, leading to increased emission and pulsations at X-ray, UV, and optical frequencies. The system switches back to the high mode. This scenario is supported by the modelling of the SEDs extracted separately during the high and low modes.

• Relativistic pulsar winds can shape the structure and dynamics of accretion flows in X-ray binary systems containing quickly spinning NSs, and can be used to probe emission mechanisms in tMSPs and other X-ray binary systems.

• tMSPs and black-hole systems share intriguing similarities in their phenomenological properties, emphasizing the need for further research to deepen our understanding of accretion physics in compact objects.

Upon request, the corresponding authors (MCB and FCZ) will provide the code used to produce the figures.

References

Ahn, C. P., Alexandroff, R., Allende Prieto, C., et al. 2014, ApJS, 211, 17
Andersen, B. C. & Ransom, S. M. 2018, ApJ, 863, L13
Appenzeller, I., Fricke, K., Fürtig, W., et al. 1998, The Messenger, 94, 1
Archibald, A. M., Bogdanov, S., Patruno, A., et al. 2015, ApJ, 807, 62
Archibald, A. M., Kaspi, V. M., Hessels, J. W. T., et al. 2013, arXiv e-prints, arXiv:1311.5161
Archibald, A. M., Stairs, I. H., Ransom, S. M., et al. 2009, Science, 324, 1411
Arnaud, K. A. 1996, in Astronomical Data Analysis Software and Systems V, Vol. 101, XSPEC: The First Ten Years, ed. G. H. Jacoby & J. Barnes (ASP, San Francisco), 17–20
Astropy Collaboration, Price-Whelan, A. M., Lim, P. L., et al. 2022, ApJ, 935, 167
Astropy Collaboration, Price-Whelan, A. M., Sipőcz, B. M., et al. 2018, aj, 156, 123
Astropy Collaboration, Robitaille, T. P., Tollerud, E. J., et al. 2013, A&A, 558, A33
Baglio, M. C., D'Avanzo, P., Campana, S., et al. 2016, A&A, 591, A101
Baglio, M. C., Mainetti, D., D'Avanzo, P., et al. 2014, A&A, 572, A99
Baglio, M. C., Russell, D. M., Casella, P., et al. 2018, ApJ, 867, 114
Baglio, M. C., Russell, D. M., Crespi, S., et al. 2020, ApJ, 905, 87
Baglio, M. C., Vincentelli, F., Campana, S., et al. 2019, A&A, 631, A104
Belloni, T., Méndez, M., King, A. R., van der Klis, M., & van Paradijs, J. 1997, ApJ, 479, L145
Berry, D., Graves, S., Bell, G. S., et al. 2022, in Astronomical Society of the Pacific Conference Series, Vol. 532, Astronomical Society of the Pacific Conference Series, ed. J. E. Ruiz, F. Pierfederici, & P. Teuben, 559
Bogdanov, S., Deller, A. T., Miller-Jones, J. C. A., et al. 2018, ApJ, 856, 54
Bogovalov, S. V. 1999, A&A, 349, 1017
Briggs, D. S. 1995, PhD thesis, New Mexico Institute of Mining and Technology, United States
Burgay, M., Burderi, L., Possenti, A., et al. 2003, ApJ, 589, 902
Burrows, D. N., Hill, J. E., Nousek, J. A., et al. 2005, Space Science Reviews, 120, 165
Burtovoi, A., Zampieri, L., Fiori, M., et al. 2020, MNRAS, 498, L98
Campana, S. & Di Salvo, T. 2018, in Astrophysics and Space Science Library, Vol. 457, Astrophysics and Space Science Library, ed. L. Rezzolla, P. Pizzochero, D. I. Jones, N. Rea, & I. Vidaña, 149
Campana, S., Miraval Zanon, A., Coti Zelati, F., et al. 2019, A&A, 629, L8
Cardelli, J. A., Clayton, G. C., & Mathis, J. S. 1989, ApJ, 345, 245
CASA Team, Bean, B., Bhatnagar, S., et al. 2022, PASP, 134, 114501
Chakrabarty, D. 1998, ApJ, 492, 342
Chaty, S., Dubus, G., & Raichoor, A. 2011, A&A, 529, A3
Chevalier, R. A. 1998, ApJ, 499, 810
Coti Zelati, F., Baglio, M. C., Campana, S., et al. 2014, MNRAS, 444, 1783
Coti Zelati, F., Campana, S., Braito, V., et al. 2018, A&A, 611, A14
Covino, S., Lazzati, D., Ghisellini, G., et al. 1999, A&A, 348, L1
Covino, S., Zerbi, F. M., Chincarini, G., et al. 2004, Astronomische Nachrichten, 325, 543
Currie, M. J., Berry, D. S., Jenness, T., et al. 2014, in Astronomical Society of the Pacific Conference Series, Vol. 485, Astronomical Data Analysis Software and Systems XXIII, ed. N. Manset & P. Forshay, 391
de Haas, S. E. M., Russell, T. D., Degenaar, N., et al. 2021, MNRAS, 502, 521
Deller, A. T., Camilo, F., Reynolds, J. E., & Halpern, J. P. 2012, ApJ, 748, L1
Deller, A. T., Moldon, J., Miller-Jones, J. C. A., et al. 2015, ApJ, 809, 13
di Serego Alighieri, S. 1998, Cambridge University Press, 199, 287
Díaz Trigo, M., Altamirano, D., Dinçer, T., et al. 2018, A&A, 616, A23
Díaz Trigo, M., Migliari, S., Miller-Jones, J. C. A., et al. 2017, A&A, 600, A8
Díaz Trigo, M., Petry, D., Humphreys, E., Impellizzeri, C. M. V., & Liu, H. B. 2021, A&A, 650, A37
Egron, E., Pellizzoni, A., Righini, S., et al. 2021, ApJ, 906, 10
Evans, P. A., Beardmore, A. P., Page, K. L., et al. 2009, MNRAS, 397, 1177
Fender, R. & Bright, J. 2019, MNRAS, 489, 4836
Fender, R., Spencer, R., Tzioumis, T., et al. 1998, ApJ, 506, L121
Fender, R. P., Belloni, T. M., & Gallo, E. 2004, MNRAS, 355, 1105
Fender, R. P., Hjellming, R. M., Tilanus, R. P. J., et al. 2001, MNRAS, 322, L23
Fender, R. P., Mooley, K. P., Motta, S. E., et al. 2023, MNRAS, 518, 1243
Fender, R. P., Pooley, G. G., Durouchoux, P., Tilanus, R. P. J., & Brocksopp, C. 2000, MNRAS, 312, 853
Foight, D. R., Güver, T., Özel, F., & Slane, P. O. 2016, ApJ, 826, 66
Foreman-Mackey, D. 2016, The Journal of Open Source Software, 1, 24
Fruscione, A., McDowell, J. C., Allen, G. E., et al. 2006, in SPIE Conference Series, Vol. 6270, Observatory Operations: Strategies, Processes, and Systems, ed. D. R. Silva & R. E. Doxsey (SPIE, Bellingham), 62701V
Gabriel, C., Denby, M., Fyfe, D. J., et al. 2004, in Astronomical Data Analysis Software and Systems (ADASS) XIII, Vol. 314, The XMM-Newton SAS - Distributed Development and Maintenance of a Large Science Analysis System: A Critical Analysis, ed. F. Ochsenbein, M. G. Allen, & D. Egret (San Francisco, CA: ASP), 759
Gallo, E., Degenaar, N., & van den Eijnden, J. 2018, MNRAS, 478, L132
Gandhi, P. 2009, ApJ, 697, L167
Gandhi, P., Dhillon, V. S., Durant, M., et al. 2010, MNRAS, 407, 2166
Gehrels, N., Chincarini, G., Giommi, P., et al. 2004, ApJ, 611, 1005
Gendreau, K. C., Arzoumanian, Z., & Okajima, T. 2012, in Society of Photo-Optical Instrumentation Engineers (SPIE) Conference Series, Vol. 8443, Space Telescopes and Instrumentation 2012: Ultraviolet to Gamma Ray, ed. T. Takahashi, S. S. Murray, & J.-W. A. den Herder, 844313
Ghedina, A., Ambrosino, F., Cecconi, M., et al. 2022, in Society of Photo-Optical Instrumentation Engineers (SPIE) Conference Series, Vol. 12184, Ground-based and Airborne Instrumentation for Astronomy IX, ed. C. J. Evans, J. J. Bryant, & K. Motohara, 121847U
Hakala, P. & Kajava, J. J. E. 2018, MNRAS, 474, 3297
Hales, C. A. 2016, invgain v1.3
Harris, C. R., Millman, K. J., van der Walt, S. J., et al. 2020, Nature, 585, 357
Harrison, F. A., Craig, W. W., Christensen, F. E., et al. 2013, ApJ, 770, 103
Henden, A. A. 2019, Journal of the American Association of Variable Star Observers (JAAVSO), 47, 130
Hogg, D. W. & Foreman-Mackey, D. 2018, ApJS, 236, 11
Homan, J., Bright, J., Motta, S. E., et al. 2020, ApJ, 891, L29
Hotan, A. W., van Straten, W., & Manchester, R. N. 2004, PASA, 21, 302
Hunter, J. D. 2007, Computing in Science & Engineering, 9, 90
Iacolina, M. N., Burgay, M., Burderi, L., Possenti, A., & di Salvo, T. 2009, A&A, 497, 445
Illiano, G., Papitto, A., Ambrosino, F., et al. 2023, A&A, 669, A26
Jansen, F., Lumb, D., Altieri, B., et al. 2001, A&A, 365, L1
Jaodand, A. D., Hernández Santisteban, J. V., Archibald, A. M., et al. 2021, arXiv e-prints, arXiv:2102.13145
Jiang, P., Tang, N.-Y., Hou, L.-G., et al. 2020, Research in Astronomy and Astrophysics, 20, 064
Jiang, P., Yue, Y., Gan, H., et al. 2019, Science China Physics, Mechanics, and Astronomy, 62, 959502
Joye, W. A. & Mandel, E. 2003, in Astronomical Society of the Pacific Conference Series, Vol. 295, Astronomical Data Analysis Software and Systems XII, ed. H. E. Payne, R. I. Jedrzejewski, & R. N. Hook, 489
Kelly, B. C. 2007, ApJ, 665, 1489
Kennedy, M. R., Clark, C. J., Voisin, G., & Breton, R. P. 2018, MNRAS, 477, 1120
Koljonen, K. I. I. & Hovatta, T. 2021, A&A, 647, A173
Linares, M., De Marco, B., Wijnands, R., & van der Klis, M. 2022, MNRAS, 512, 5269
Lucy, L. B. 2016, A&A, 588, A19
Manchester, R. N., Hobbs, G. B., Teoh, A., & Hobbs, M. 2005, AJ, 129, 1993
Mason, K. O., Breeveld, A., Much, R., et al. 2001, A&A, 365, L36
Méndez, M., Karpouzas, K., García, F., et al. 2022, Nature Astronomy
Migliari, S., Fender, R. P., Rupen, M., et al. 2004, MNRAS, 351, 186
Miraval Zanon, A., Ambrosino, F., Coti Zelati, F., et al. 2022, A&A, 660, A63
Moorwood, A., Cuby, J. G., & Lidman, C. 1998, The Messenger, 91, 9
Motta, S. E., Rodriguez, J., Jourdain, E., et al. 2021, New A Rev., 93, 101618
Nandra, K., Barret, D., Barcons, X., et al. 2013, arXiv e-prints, arXiv:1306.2307
Narayan, R. & Yi, I. 1994, ApJ, 428, L13
Nasa High Energy Astrophysics Science Archive Research Center (Heasarc). 2014, HEAsoft: Unified Release of FTOOLS and XANADU
Ogley, R. N., Bell Burnell, S. J., Fender, R. P., Pooley, G. G., & Waltman, E. B. 2000, MNRAS, 317, 158
Papitto, A., Ambrosino, F., Stella, L., et al. 2019, ApJ, 882, 104
Papitto, A. & de Martino, D. 2022, in Astrophysics and Space Science Library, Vol. 465, Astrophysics and Space Science Library, ed. S. Bhattacharyya, A. Papitto, & D. Bhattacharya, 157–200
Papitto, A., Rea, N., Coti Zelati, F., et al. 2018, ApJ, 858, L12
Paredes, J. M., Martí, J., Peracaula, M., Pooley, G., & Mirabel, I. F. 2000, A&A, 357, 507
Patruno, A., Archibald, A. M., Hessels, J. W. T., et al. 2014, ApJ, 781, L3
Qian, L., Yao, R., Sun, J., et al. 2020, The Innovation, 1, 100053
Ransom, S. M. 2001, PhD thesis, Harvard University
Ray, P. S., Arzoumanian, Z., Ballantyne, D., et al. 2019, arXiv e-prints, arXiv:1903.03035
Robitaille, T. & Bressert, E. 2012, APLpy: Astronomical Plotting Library in Python
Roming, P. W. A., Kennedy, T. E., Mason, K. O., et al. 2005, Space Science Reviews, 120, 95
Russell, D. M. & Fender, R. P. 2008, MNRAS, 387, 713
Russell, D. M., Markoff, S., Casella, P., et al. 2013a, MNRAS, 429, 815
Russell, D. M., Russell, T. D., Miller-Jones, J. C. A., et al. 2013b, ApJ, 768, L35
Russell, D. M., Russell, T. D., Miller-Jones, J. C. A., et al. 2013c, ApJ, 768, L35

Russell, D. M., Shahbaz, T., Lewis, F., & Gallo, E. 2016, MNRAS, 463, 2680
Russell, T. D., Lucchini, M., Tetarenko, A. J., et al. 2020, MNRAS, 498, 5772
Russell, T. D., Tetarenko, A. J., Miller-Jones, J. C. A., et al. 2019, ApJ, 883, 198
Saikia, P., Russell, D. M., Baglio, M. C., et al. 2022, ApJ, 932, 38
Schartel, N., González-Riestra, R., Kretschmar, P., et al. 2022, XMM-Newton
Serkowski, K., Mathewson, D. S., & Ford, V. L. 1975, ApJ, 196, 261
Shahbaz, T. 2019, in Astrophysics and Space Science Library, Vol. 460, Astronomical Polarisation from the Infrared to Gamma Rays, ed. R. Mignani, A. Shearer, A. Słowikowska, & S. Zane, 247
Shahbaz, T., Dallilar, Y., Garner, A., et al. 2018, MNRAS, 477, 566
Shahbaz, T., González-Hernández, J. I., Breton, R. P., et al. 2022, MNRAS, 513, 71
Shahbaz, T., Linares, M., Nevado, S. P., et al. 2015, MNRAS, 453, 3461
Shahbaz, T., Linares, M., Rodríguez-Gil, P., & Casares, J. 2019, MNRAS, 488, 198
Soffitta, P., Baldini, L., Bellazzini, R., et al. 2021, AJ, 162, 208
Stappers, B. W., Archibald, A. M., Hessels, J. W. T., et al. 2014, ApJ, 790, 39
Stella, L. & Angelini, L. 1992, in Astronomical Society of the Pacific Conference Series, Vol. 25, Astronomical Data Analysis Software and Systems I, ed. D. M. Worrall, C. Biemesderfer, & J. Barnes, 103
Stetson, P. B. 1987a, PASP, 99, 191
Stetson, P. B. 1987b, PASP, 99, 191
Strüder, L., Briel, U., Dennerl, K., et al. 2001, A&A, 365, L18
Tetarenko, A. J., Casella, P., Miller-Jones, J. C. A., et al. 2021, MNRAS, 504, 3862
Tetarenko, A. J., Sivakoff, G. R., Miller-Jones, J. C. A., et al. 2019, MNRAS, 482, 2950
Tetarenko, A. J., Sivakoff, G. R., Miller-Jones, J. C. A., et al. 2015, ApJ, 805, 30
Tetarenko, A. J., Sivakoff, G. R., Miller-Jones, J. C. A., et al. 2017, MNRAS, 469, 3141
Turner, M. J. L., Abbey, A., Arnaud, M., et al. 2001, A&A, 365, L27
Ueda, Y., Yamaoka, K., Sánchez-Fernández, C., et al. 2002, ApJ, 571, 918
van den Eijnden, J., Degenaar, N., Russell, T. D., et al. 2021, MNRAS, 507, 3899
van der Horst, A. J., Curran, P. A., Miller-Jones, J. C. A., et al. 2013, MNRAS, 436, 2625
van der Laan, H. 1966, Nature, 211, 1131
Vaughan, B. A., van der Klis, M., Wood, K. S., et al. 1994, ApJ, 435, 362
Vaughan, S., Edelson, R., Warwick, R. S., & Uttley, P. 2003, MNRAS, 345, 1271
Veledina, A., Nättilä, J., & Beloborodov, A. M. 2019, ApJ, 884, 144
Verbunt, F. 1993, ARA&A, 31, 93
Virtanen, P., Gommers, R., Oliphant, T. E., et al. 2020, Nat. Methods, 17, 261
Wang, P., Li, D., Clark, C. J., et al. 2021, Science China Physics, Mechanics, and Astronomy, 64, 129562
Weisskopf, M. C., Ramsey, B., O'Dell, S., et al. 2016, in Society of Photo-Optical Instrumentation Engineers (SPIE) Conference Series, Vol. 9905, Space Telescopes and Instrumentation 2016: Ultraviolet to Gamma Ray, ed. J.-W. A. den Herder, T. Takahashi, & M. Bautz, 990517
Weng, S.-S., Qian, L., Wang, B.-J., et al. 2022, Nature Astronomy, 6, 698
Wood, C. M., Miller-Jones, J. C. A., Homan, J., et al. 2021, MNRAS, 505, 3393
Woodgate, B. E., Kimble, R. A., Bowers, C. W., et al. 1998, PASP, 110, 1183
Zerbi, R. M., Chincarini, G., Ghisellini, G., et al. 2001, Astronomische Nachrichten, 322, 275
Zhang, S. N., Feroci, M., Santangelo, A., et al. 2016, in Society of Photo-Optical Instrumentation Engineers (SPIE) Conference Series, Vol. 9905, Space Telescopes and Instrumentation 2016: Ultraviolet to Gamma Ray, ed. J.-W. A. den Herder, T. Takahashi, & M. Bautz, 99051Q

Appendix A: Searches for counterparts to ALMA J102349.1+003824

We searched for a counterpart to ALMA J102349.1+003824 at other wavelengths using both simultaneous and archival observations of the field. No UV emission was detected at the source position in the *Swift*/UVOT observations simultaneous with ALMA, either in the images collected separately during the three snapshots, or in the stack of these images. We set a 3σ upper limit on the magnitude of a putative counterpart of UVM2>21 from the stacked image (total exposure of ~ 2.4 ks). A few weeks before the ALMA observations were acquired, the field of view of ALMA J102349.1+003824 was also observed in the optical (g', r' and i' SDSS filters) with the Las Cumbres Observatory (LCO) network of telescopes. No counterpart was detected in these data. We set the following 3σ upper limits on the optical magnitude using 60-s images acquired with the 1m telescope of the LCO network located in South Africa on May 8, 2021: $i' > 17.8$, $r' > 17.9$, $g' > 18.6$. There is also no optical/NIR counterpart in either the third data release (DR3) from the *Gaia* space telescope or in the 2MASS point source catalog. ALMA J102349.1+003824 was also not detected in the VLA observation carried out a few weeks earlier, down to a 3-σ flux density upper limit of $12\,\mu$Jy at 10 GHz.

Several observations of the field have been performed in the soft X-ray band over the past years, mainly using *Swift* and *XMM-Newton*. However, given the X-ray luminosity of J1023 and its small angular distance from ALMA J102349.1+003824, the point-spread function of the X-ray instruments on board these observatories encompasses the position of ALMA J102349.1+003824, preventing a conclusive assessment of the presence or absence of an X-ray counterpart to this source. We then analyzed a 83-ks long *Chandra*/ACIS-S observation performed in March 2011 (Obs. ID 11075) to search for X-ray emission at the position of ALMA J102349.1+003824. We reprocessed the data using the task CHANDRA_REPRO within the CIAO software and ran the WAVDETECT source detection tool. No evidence for an X-ray counterpart to ALMA J102349.1+003824 was found. Using SRCFLUX, we set a 3σ upper limit on the net count rate of 1.3×10^{-4} counts s^{-1} over the 0.5–7.0 keV energy range. Assuming an absorbed power-law spectrum with an absorption column density of $N_{\rm H} = 5 \times 10^{20}$ cm^{-2} (i.e., the one expected within the Galaxy in the direction of the source: **?**) and photon index in the range $\Gamma = 1 - 4$, the limit above translates into an unabsorbed flux of $< (2-4) \times 10^{-15}$ erg cm^{-2} s^{-1} (depending on the assumed power-law slope) in the 0.5–7 keV range.